Slab melting and magma formation beneath the southern Cascade arc

Elsevier Editorial System(tm) for Earth and Planetary Science Letters

Manuscript Draft

Manuscript Number: EPSL-D-15-01035R2

Title: Slab melting and magma formation beneath the southern Cascade Arc

Article Type: Letters

Keywords: Subduction zone; Volatiles; Cascades; Melt inclusions; Geochemistry; Arc

Corresponding Author: Dr. Kristina J Walowski, Ph.D.

Corresponding Author's Institution: University of Edinburgh

First Author: Kristina J Walowski, Ph.D.

Order of Authors: Kristina J Walowski, Ph.D.; Paul J Wallace, Ph.D.; Michael A Clynne, Ph.D.; Daniel J Rasmussen, M.S.; Dominique Weis, Ph.D.

Abstract: The processes that drive magma formation beneath the Cascade arc and other warm-slab subduction zones have been debated because young oceanic crust is predicted to largely dehydrate beneath the forearc during subduction. In addition, geochemical variability along strike in the Cascades has led to contrasting interpretations about the role of volatiles in magma generation. Here, we focus on the Lassen segment of the Cascade arc, where previous work has demonstrated across-arc geochemical variations related to subduction enrichment, and H-isotope data suggest that H2O in basaltic magmas is derived from the final breakdown of chlorite in the mantle portion of the slab. We use naturally glassy, olivine-hosted melt inclusions from the tephra deposits of eight primitive (MgO > 7 wt%) basaltic cinder cones to quantify the pre-eruptive volatile contents of mantle-derived melts in this region. The melt inclusions have B concentrations and isotope ratios that are similar to mid-ocean ridge basalt (MORB), suggesting extensive dehydration of the downgoing plate prior to reaching sub-arc depths and little input of slab-derived B into the mantle wedge. However, correlations of volatile and trace element ratios (H2O/Ce, Cl/Nb, Sr/Nd) in the melt inclusions demonstrate that geochemical variability is the result of variable addition of a hydrous subduction component to the mantle wedge. Furthermore, correlations between subduction component tracers and radiogenic isotope ratios show that the subduction component has less radiogenic Sr and Pb than the Lassen sub-arc mantle, which can be explained by melting of subducted Gorda MORB beneath the arc. Agreement between pMELTS melting models and melt inclusion volatile, major, and trace element data suggests that hydrous slab melt addition to the mantle wedge can produce the range in primitive compositions erupted in the Lassen region. Our results provide further evidence that chlorite-derived fluids from the mantle portion of the slab (~7-9 km below the slab top) cause flux melting of the subducted oceanic crust, producing hydrous slab melts that migrate into the overlying mantle, where they react with peridotite to induce further melting.

Slab melting and magma formation beneath the southern Cascade Arc

Walowski, K.J. [1,2]*, Wallace, P.J. [1], Clynne, M.A. [3], Rasmussen, D.J. [4], Weis, D. [5]

[1] University of Oregon, Department of Geological Sciences, Eugene, OR, USA

[2] University of Edinburgh, School of Geosciences, Grant Institute, Edinburgh, UK

[3] United States Geological Survey, Volcano Science Center, Menlo Park, CA, USA

[4] Lamont Doherty Earth Observatory, Palisades, NY, USA

[5] University of British Columbia, Earth, Ocean, and Atmospheric Science Department, Vancouver, BC, Canada

*Corresponding Author - Current contact information: k.walowski@ed.ac.uk

Keywords: Subduction zone; Volatiles; Cascades; Melt inclusions; GeocheMIstry; Arc

Abstract

The processes that drive magma formation beneath the Cascade arc and other warm-slab subduction zones have been debated because young oceanic crust is predicted to largely dehydrate beneath the forearc during subduction. In addition, geochemical variability along strike in the Cascades has led to contrasting interpretations about the role of volatiles in magma generation. Here, we focus on the Lassen segment of the Cascade arc, where previous work has demonstrated across-arc geochemical variations related to subduction enrichment, and H-isotope

data suggest that H_2O in basaltic magmas is derived from the final breakdown of chlorite in the mantle portion of the slab. We use naturally glassy, olivine-hosted melt inclusions (MI) from the tephra deposits of eight primitive (MgO > 7 wt%) basaltic cinder cones to quantify the pre-eruptive volatile contents of mantle-derived melts in this region. The melt inclusions have B concentrations and isotope ratios that are similar to mid-ocean ridge basalt (MORB), suggesting extensive dehydration of the downgoing plate prior to reaching sub-arc depths and little input of slab-derived B into the mantle wedge. However, correlations of volatile and trace element ratios (H_2O/Ce, Cl/Nb, Sr/Nd) in the melt inclusions demonstrate that geochemical variability is the result of variable addition of a hydrous subduction component to the mantle wedge. Furthermore, correlations between subduction component tracers and radiogenic isotope ratios show that the subduction component has less radiogenic Sr and Pb than the Lassen sub-arc mantle, which can be explained by melting of subducted Gorda MORB beneath the arc. Agreement between pMELTS melting models and melt inclusion volatile, major, and trace element data suggests that hydrous slab melt addition to the mantle wedge can produce the range in primitive compositions erupted in the Lassen region. Our results provide further evidence that chlorite-derived fluids from the mantle portion of the slab (~7-9 km below the slab top) cause flux melting of the subducted oceanic crust, producing hydrous slab melts that migrate into the overlying mantle, where they react with peridotite to induce further melting.

1. Introduction

47

48 Dehydration of subducted oceanic lithosphere drives arc magmatism at
49 convergent plate margins. However, the thermal structure of an individual
50 subduction zone controls the depths at which key dehydration reactions occur
51 (Schmidt and Poli, 1998; Van Keken et al., 2011). Thermal structure is commonly
52 assessed using the thermal parameter (ϕ), which is a function of downgoing plate
53 age, dip angle, and convergence rate (e.g., Syracuse et al., 2010). Variability in ϕ
54 globally is predicted to cause a wide range of slab surface temperatures beneath
55 arcs (675-950°C), as estimated from geodynamic models (e.g., Syracuse et al., 2010)
56 and geochemical tools (e.g., Cooper et al., 2012). The results suggest a continuum of
57 subduction zones between 'cold' (Tonga, Kamchatka) and 'warm' slabs (Cascades,
58 Mexico). Fluids released from the subducting slab have been shown to become more
59 solute-rich with increased temperature (Kessel et al., 2005a; Herman and Spandler,
60 2006; Cooper et al., 2012; Ruscitto et al., 2012), and there is geochemical evidence
61 for melting of the oceanic crust beneath some warm-slab endmembers such Mexico
62 (Cai et al., 2014), the Cascades (Walowski et al., 2015), and SW Japan (Kimura et al.,
63 2014). In addition, there is widespread geochemical evidence for melting of
64 subducted sediment beneath arcs (e.g., Plank et al., 2005). However, whether the
65 oceanic crust begins to melt beneath most arcs has been debated, and a consensus is
66 emerging that the oceanic crust dehydrates and contributes fluids to the mantle
67 wedge in arcs with cold to intermediate slab temperatures (e.g., van Keken et al.,
68 2011). To understand slab recycling and magma generation, it is imperative to
69 differentiate the roles of different components in the subducted oceanic lithosphere

(altered oceanic crust, sediment, serpentinized peridotite) and determine how these components are transferred to the overlying mantle wedge (as fluids, melts or a supercritical phase). The Cascade arc represents a global warm-slab endmember due to slow, shallow subduction of young oceanic crust (6-10 Ma at the trench; Wilson et al., 2002). Geodynamic models (Syracuse et al., 2010; Wada and Wang, 2009) and geochemical studies (Cooper et al., 2012; Ruscitto et al., 2012; Walowski et al., 2015) agree that slab surface temperatures beneath the arc axis are hotter, on average, than many other arcs globally. Previous work in the central Oregon Cascades has suggested that the mantle wedge beneath the arc receives a reduced flux of volatiles from the downgoing slab (Ruscitto et al., 2012), and H_2O concentrations in olivine-hosted melt inclusions (MI) from both the central and southern Cascades (~3.2 wt%; Ruscitto et al., 2010, 2011; LeVoyer et al., 2010) fall slightly below the global average (~3.9 wt%; Plank et al., 2013). Walowski et al. (2015) found that hydrogen isotope ratios of primitive magmas from the Lassen region of the southern Cascades are lighter than those for the Mariana arc. This is likely the result of waning dehydration of chlorite in the mantle portion of the downgoing slab (~7-9 km below the slab top) after the crustal portion of the slab has already dehydrated beneath the forearc. These results also provide evidence that flux-melting of the oceanic crust occurs when fluids released from the slab interior interact with oceanic crust that is above its wet solidus temperature (e.g., Spandler and Pirard, 2013).

We measured the volatile contents, major element, trace element, and B isotope compositions of olivine-hosted MI and the radiogenic isotopic compositions

93 of bulk tephra from the eruptive centers in the Lassen region studied by Walowski
94 et al. (2015). We use these data to quantify the chemical contributions from the
95 subducting oceanic lithosphere and to better understand how subduction of warm
96 oceanic crust affects the composition of mantle melts and the productivity of
97 melting in the mantle wedge. We also test the hypothesis of Walowski et al. (2015)
98 that magma production beneath the southern Cascades involves a multi-stage
99 process that includes flux melting of the subducted oceanic crust and hydrous slab
100 melt addition to the overlying mantle wedge.
101
102 **2. Geologic Setting**
103 The Lassen region is the southern terminus of the active Cascade arc
104 (Guffanti et al., 1990). Volcanism is the result of oblique subduction of the Gorda
105 micro-plate beneath the North American plate (Fig. 1; Wilson, 2002), producing
106 dominantly calc-alkaline magmas (Clynne and Muffler, 2010). Westward expansion
107 of the Basin and Range extensional province into the eastern flanks of the Cascade
108 arc, including the Hat Creek and Lake Almanor Grabens, has produced many normal
109 faults that provide pathways for mafic magmas to reach the surface (Guffanti et al.,
110 1990; Clynne and Muffler, 2010). The Quaternary volcanics in the Lassen region sit
111 above a broad platform of mafic to intermediate volcanoes and volcanic products 2-
112 4 km thick (Berge and Stauber, 1987), which is underlain by Sierran and Klamath
113 metamorphic/plutonic basement rocks (Berge and Stauber, 1987). Surrounding the
114 Lassen Peak dacitic dome complex (Clynne and Muffler, 2010) is a large volcanic
115 field containing over 500 cinder cones and small shield volcanoes erupted in the last

12 Ma (Guffanti et al., 1990). Previous work on the Quaternary mafic volcanoes has identified a range in compositions from low-K tholeiitic basalts (LKT; also called high-alumina olivine tholeiites, or HAOT) to calc-alkaline basalt, basaltic andesite, and andesite (Clynne, 1993; Borg et al., 1997). The most primitive calc-alkaline volcanic rocks show distinct across-arc geochemical variations that are interpreted to result from variable enrichment of the sub-arc mantle by a subduction component (Fig. 1; Borg et al., 1997, 2002). Figure 1 shows variations in both Sr/Nd and $^{87}Sr/^{86}Sr$ with increasing distance from the trench. Because there is no evidence for plagioclase fractionation in the primitive magmas, these ratios are robust indicators of subduction enrichment (Borg et al., 1997; see Supplementary Discussion and Fig. S2 for details). The pattern of variable Sr/Nd in the forearc and decreasing and consistently low values of Sr/Nd in the back-arc has been interpreted to indicate the waning addition of a subduction component with distance from the trench (Borg et al., 1997). The $^{87}Sr/^{86}Sr$ ratios display an opposite pattern and generally increase toward the back-arc, indicating that the subduction component has a less radiogenic Sr isotope signature than the sub-arc mantle, which is unusual for arc volcanoes (e.g., Turner and Langmuir, 2015). Variability in whole-rock Nb/Zr and mineral cheMItry (olivine and spinel) suggests that the Lassen sub-arc mantle is heterogeneous before any slab addition (Supplementary Fig. S1; Clynne, 1993; Borg et al., 1997; Walowski et al., 2015), but there is no systematic variation of Nb/Zr with distance from the trench. A full summary of geochemical variations can be found in the Supplementary Materials, and a detailed review is provided by Borg et al. (2002).

139

140 **3. Sample Descriptions and Analytical Methods**

141

142 Samples were collected from the tephra deposits of Quaternary monogenetic
143 vents spanning ~80 km from the forearc to the back-arc (Fig. 1). Vents that erupted
144 primitive basalt or basaltic andesite (MgO > 7 wt%) identified from bulk rock
145 analyses (Clynne, 1993; Borg et al., 1997) were targeted because they are close in
146 composition to primary mantle melts. Coarse ash was collected to minimize the
147 potential for syn-eruptive diffusive H loss (e.g., Lloyd, 2013) or crystallization of
148 melt inclusions. Loose olivine crystals (250 μm to 1 mm) were hand-picked from
149 sieved tephra, treated in HBF_4 to remove adhering glass, and examined in
150 immersion oil to locate MI. Olivine crystals hosting fully enclosed, glassy MI were
151 mounted in acetone-soluble resin on glass slides and prepared as doubly polished
152 wafers. H_2O and CO_2 concentrations of the MI were measured at the University of
153 Oregon using a Thermo-Nicolet Nexus 670 FTIR spectrometer interfaced with a
154 Continuum IR microscope. Concentrations were calculated from IR peak
155 absorbances using the Beer–Lambert law and compositionally appropriate
156 absorption coefficients (see Johnson et al., 2008). MI and host olivine were analyzed
157 for major elements (plus S and Cl for inclusions) on the Cameca SX-100 electron
158 microprobe at the University of Oregon (see Ruscitto et al., 2010, for details). MI
159 were subsequently analyzed for a suite of trace elements on the Photon Machines
160 Analyte G2 135 nm ArF "fast"Excimer Laser system at Oregon State University,
161 using 50 μm spot size with a 5 Hz pulse rate. Measured trace element concentrations

were determined by reference to GSE-1G glass as a calibration standard and using 43Ca as an internal standard (see Loewen and Kent, 2012). BHVO-2G, BCR-2G, and GSD-1G glasses were also analyzed to monitor accuracy and precision, and the analyzed values were within 10% of accepted values (see Supplementary Table S5).

A subset of the MI that were analyzed for H isotopes and trace elements by Walowski et al. (2015) were also analyzed for B isotope ratios using the Cameca IMS 1280 at Woods Hole Oceanographic Institution, with O^- primary beam, 30 nA primary current, 10,000 V secondary voltage, and a 20 μm spot size. More detailed methods are described in Marschall and Monteleone (2014) and Supplementary Table S3. Some of the MI were too small to allow a new SIMS spot adjacent to an existing NanoSIMS spot (20x20 rastered area, ~5 μm deep). In these cases, the SIMS spot was placed within the pre-existing NanoSIMS spot. Tests comparing measurements within pre-existing spots to those on a clean surface from a single MI revealed no systematic differences.

The Sr, Nd, Hf, and Pb isotope ratios of bulk tephra samples were measured at the Pacific Centre for Isotopic and Geochemical Research at the University of British Columbia. Pb, Nd, and Hf isotope ratios were measured by MC-ICP-MS (Nu Instruments Ltd., Nu Plasma II NP 214), and Sr isotope ratios were measured by Thermo Finnigan Triton TIMS using procedures described in Weis et al. (2006, 2007). Additional details regarding sample preparation and analytical techniques are given by Mullen and Weis (2015). Analytical reproducibility and correction methods for radiogenic isotope data are described in Supplementary Table S2. Tephra from sample CC was excluded from isotopic analyses because of clear

185 evidence for crustal contamination (abundant quartz xenocrysts, partially melted
186 granitic xenoliths).
187
188 **4. Results**
189 **4.1 MI major and trace element compositions**
190 The olivine host crystals vary from Fo_{83} to Fo_{90} (Supplementary Table S1 and
191 S7). For each cinder cone, 11-17 MI were analyzed. The major element compositions
192 of the inclusions were corrected for post-entrapment crystallization (PEC) and Fe-
193 loss using Petrolog 3.1.1.3 (Danyushevsky and Plechov, 2011), using models for
194 olivine-melt equilibria from Ford et al. (1983) and oxidation state from Borisov and
195 Shapkin (1990). Concentrations of volatiles and trace elements that are
196 incompatible in the olivine hosts were corrected using the Petrolog results for the
197 major elements. Initial Fe contents were chosen based either on the FeO^T of the bulk
198 tephra or the highest value of FeO^T for MI from a particular cone. An average oxygen
199 fugacity of ΔQFM+1, determined using the partitioning of V between the MI and host
200 olivine using methods of Mallmann and O'Neill (2009), was used in the Petrolog
201 calculations. Calculated values of PEC vary from 0 to 14%. Corrected MI
202 compositions overlap with the most primitive lavas previously analyzed in the
203 Lassen region (Fig. 2) and have MgO concentrations of 7.4-9.8 wt% (Supplementary
204 Table S1). To estimate a primary melt composition for each cone, we added
205 equilibrium olivine (in 0.1 wt% increments) to the average MI composition from
206 each cone until the melt composition was in equilibrium with Fo_{90} olivine (Table 1;
207 Ruscitto et al., 2010). The calculated primary melt compositions required 1-20%

olivine addition (Table 1). Although variability in mantle olivine compositions likely exists beneath the Lassen region (Clynne, 1993; Borg et al., 1997), we assume Fo_{90} for simplicity and because there is little evidence for more refractory mantle compositions, unlike the Mt. Shasta region to the north, where some lavas and tephra have olivine up to Fo_{94} (Ruscitto et al., 2011).

The MI are dominantly medium-K CAB, with some that fall into the low-K field (Fig. 2a), and compositionally similar to the bulk tephra compositions (Walowski et al., 2015; Supplementary Fig. S2). Previous work in the Lassen region has suggested that LKT and CAB magmas have different source regions (Clynne, 1993; Bacon et al., 1997). However, the low-K samples used in this study do not display the lower LREE/HREE and LILE/HFSE values typical of the endmember LKT volcanic rocks in this region (Fig. 2; see also Bacon et al., 1997). All samples used in this study display trace element patterns similar to the regional CABs (Fig. 2), suggesting that despite variability in major and trace element compositions, they were enriched by a component derived from the downgoing slab.

4.2 Magmatic volatile contents

Dissolved H_2O contents of the MI, after correction for PEC and Fe loss, are 0.6-3.5wt%. At individual cinder cones, a range in H_2O concentrations is observed and is likely due to differences in extent of pre-entrapment degassing (e.g., Johnson et al., 2009) and/or post-entrapment hydrogen loss (Lloyd et al., 2013; Bucholz et al., 2013). We do not observe correlations between relative MI size and H_2O contents. Because these processes decrease H_2O, the maximum measured H_2O/K_2O ratio for

231 each cone was used to estimate the initial H_2O content (H_2O_{max}) of the magma
232 erupted at that cone. In the Lassen region, H_2O_{max} ranges from 1.3-3.4 wt%. The
233 H_2O_{max} values were used to estimate the H_2O concentrations in primary mantle-
234 derived melts using the olivine addition method described above, yielding values of
235 1.1-3.4 wt% (Table 1). These values overlap with calculated primary melt H_2O
236 concentrations for basaltic and basaltic andesite melts from central Oregon (1.4-3.0
237 wt%; Ruscitto et al., 2010). In contrast to H_2O, Cl is not affected by either pre-
238 entrapment degassing (except at very low pressures) or post-entrapment diffusive
239 effects. Concentrations of Cl in calculated primary melts range from 100-600 ppm,
240 except at BRM, where Cl values are as high as 2500 ppm (Supplementary Table S1).
241 Similar to H_2O, CO_2 concentrations are variable at individual cones and
242 reflect a combination of pre-entrapment degassing and post-entrapment loss. We
243 report the highest PEC-corrected CO_2 contents from individual cinder cones, and
244 these range from 599-1493 ppm (Supplementary Table S1; Fo_{90} corrected primary
245 melts = 521-1435 ppm; Table 1). It is important to note that these CO_2 values
246 underestimate the initial CO_2 concentration of the melt. Most MI analyzed in this
247 study contain a vapor bubble (presence /absence of vapor bubble noted in
248 Supplementary Table S1), and such bubbles typically contain a substantial fraction
249 (40-90%) of the CO_2 that was initially dissolved in the trapped melt (Wallace et al.,
250 2015; Moore et al., 2015). As a result, the CO_2 contents of the MI are underestimates
251 of the magmatic CO_2 content. Sulfur contents of PEC corrected MI range from 380-
252 2140 ppm (Supplementary Table S4; Fo_{90} corrected primary melts = 900-1600 ppm;
253 Table 1). Samples BRVB, BPB, and BBL each have one MI that contains a small (<5

μm sphere) coexisting sulfide phase. Because post-entrapment Fe-loss can cause sulfide saturation and decreasing sulfur in the residual melt (Danyushevsky et al., 2002), these few individual MI may have lost some S after entrapment. However, there is no evidence to suggest this process had an effect on most MI, such as highly variable S contents from an individual MI suite.

4.3 Isotopic Compositions

The average $\delta^{11}B$ ratios of MI from individual cones in the Lassen region range from -9.9‰ to -2.4‰ (Fig. 3; Supplementary Table S3). These values overlap with those measured for bulk rock samples from the southern Washington Cascades (-9‰ to -0.4‰; Leeman et al., 2004) and MI from the Mt. Shasta region (Fig. 3; Rose et al., 2001; LeVoyer et al., 2010). MI from the Cascades have lower B concentrations and more negative $\delta^{11}B$ than those measured in other arcs, such as Kamchatka and Mariana, where older oceanic crust subducts (Fig. 3; Ishikawa et al., 2001; Ishikawa and Tera, 1999).

The Sr, Nd, Hf, and Pb isotope ratios for bulk tephra samples overlap with those previously determined for volcanic rocks in the Lassen Region (Fig. 4; Table 2).

5. Discussion

5.1 The source of volatiles in Lassen Region primitive magmas

Boron is a fluid mobile element that is present in higher concentrations in subducted materials than the mantle, making it an excellent tracer of fluids from subducting slabs (e.g., Tonarini et al., 2001). In addition, subducted materials such

277 as sediment, oceanic crust, and serpentinitized mantle have $\delta^{11}B$ that is distinct
278 from the mantle wedge (e.g., Ishikawa and Nakamura, 1993). However, the Lassen
279 region MI have MORB-like to slightly elevated B isotopic compositions and low B
280 concentrations, which suggests that the sub-arc mantle receives little B from the
281 subducting slab (Fig. 3). This is probably the result of extensive dehydration of the
282 slab before it reaches sub-arc depths (Leeman et al., 2004; Manea et al., 2014).
283 However, geodynamic modeling and calculated metamorphic phase equilibria
284 suggest that, unlike B, H_2O can be carried to sub-arc depths beneath the Lassen
285 region by chlorite in the hydrated mantle portion of the slab (van Keken et al., 2011;
286 Walowski et al., 2015). Because nearly all B is released from hydrated peridotite
287 beneath the forearc during antigorite breakdown, chlorite-derived fluids contribute
288 little B to the subduction component (Spandler et al., 2014). This explains how the
289 slab beneath the Cascades can release a hydrous component that contains very little
290 B, such that primitive magmas formed in the wedge have B isotope ratios and
291 concentrations only slightly elevated compared to MORB.
292 Despite low B concentrations, H_2O and Cl are high compared to MORB, which
293 requires that these volatiles are retained in the slab to greater depths than B.
294 Furthermore, strong correlations of H_2O_{max}/Ce and Cl/Nb with Sr/Nd clearly
295 demonstrate that volatile and trace element enrichments are coupled and therefore
296 derived from the same process (Fig. 5). This observation is consistent correlations
297 globally and at other warm-slab subduction zones (Ruscitto et al., 2012). To quantify
298 this, we calculated the compositions of partial melts from two mantle endmembers
299 to which variable amounts of subduction component were added. Figure 5 shows

300 good agreement between the model curves and the MI data, which indicates that
301 volatile and trace element variability between vents is the result of different
302 amounts of a subduction component added to a heterogeneous mantle wedge.
303 However, MI from cone BRM have lower H_2O/Ce than predicted by the melting
304 model. This could be caused by variability in the H_2O and trace element ratios of the
305 hydrous subduction component, or it could be that MI from this cone were strongly
306 affected by pre-entrapment degassing or post-entrapment H loss. Cl/Nb provides a
307 more robust indication of initial volatile concentration because Cl is not affected by
308 diffusive loss and only degasses at very low pressure. Good agreement between data
309 and melting models for Cl/Nb vs. Sr/Nd provides support for the interpretation that
310 initial H_2O concentrations are related to the amount of a subduction component
311 added to the mantle wedge beneath the arc and that the slab component has ratios
312 of H_2O and Cl to LILE that are not highly variable (Fig. 5b, c). This suggests that BRM,
313 the sample with the highest Sr/Nd and therefore largest amount of a subduction
314 component, has very low H_2O/Ce as a result of extensive degassing or post-
315 entrapment diffusive loss.
316 Volatile and trace element ratios for the central Oregon Cascades can also be
317 explained using the calculated melting curves, but require a more enriched mantle
318 source than Lassen magmas (Fig. 5a; Ruscitto et al., 2010). Interestingly, MI with the
319 highest values of Sr/Nd in both the Lassen region (BRM) and the Mt. Shasta region
320 do not have the highest values of H_2O/Ce, but they do have the highest Cl/Nb and
321 also have Cl concentrations significantly higher than other cones throughout the
322 Cascades (Ruscitto et al., 2012). As suggested above, these magmas likely

323 experienced extensive degassing of H_2O in the crust before MI entrapment
324 (evidenced by very low CO_2 in many MI), and/or were affected by post-entrapment
325 H loss. However, if the BRM and Shasta magmas had pre-degassing compositions
326 that fit the model curves in Figure 5a, they would have had initial H_2O
327 concentrations as high as 8-10 wt% H_2O, in agreement with experimental phase
328 equilibria (Krawczynski et al., 2012). The Blanco Fracture zone, which separates the
329 Juan de Fuca and Gorda plates, may provide a pathway for deep serpentinization of
330 the upper mantle in the downgoing slab offshore of the Cascades, and has been
331 proposed as a source for the volatile-rich component beneath Mt. Shasta (Grove et
332 al., 2002; Manea et al., 2014). However, plate reconstructions suggest the Blanco
333 Fracture zone is not old enough to project beneath the arc (Wilson, 2002), and thus,
334 the causes of geochemical differences between the Mt. Shasta and Lassen regions
335 (Fig. 5) remain enigmatic.
336
337 **5.2 The Lassen sub-arc mantle**
338 Previous workers using trace elements and radiogenic isotopes in the Lassen
339 region found negative correlations between LILE/LREE ratios and $^{87}Sr/^{86}Sr$. This
340 requires that the modern subduction component is less radiogenic than the sub-arc
341 mantle and that the latter has anomalously high Pb and Sr isotope ratios (Borg et al.,
342 1997, 2002; Fig. 4). This observation by Borg et al. (1997) led to the conclusion that
343 the sub-arc mantle had been previously enriched by a sediment component, but
344 they suggested the enrichment must have occurred during an earlier, possibly
345 Mesozoic, subduction event because the Pb isotope ratios of young Pacific sediments

were too low to explain the values. Subsequent research on sediments from the Cascadia Basin (Fig. 4a; Carpentier et al., 2014; Mullen and Weis, 2015) has shown that the sediments have radiogenic Pb isotopic ratios. Addition of such a bulk sediment to depleted MORB mantle (DMM) could explain the anomalously radiogenic Pb and Sr isotope ratios and trace element enrichments inferred for the Lassen sub-arc mantle (Fig. 4a). However, it does not resolve the questions of when or how the bulk sediment component was added, nor does it solve the puzzle evident in Figs. 1c, d, and 4a that modern subduction seems to involve addition of a less radiogenic slab component to an already isotopically enriched mantle wedge. Addition of bulk sediment rather than sediment melt could be explained by mélange diapirs that rise from the top of the subducted plate (e.g., Behn et al., 2011; Gerya et al., 2003). Interestingly, the enriched mantle signature is restricted to the southernmost Cascades, and may best be explained by either the addition of bulk sediment to the mantle wedge during the accretionary events which produced the Klamath Mountains terranes from 130-260 Ma (Irwin and Wooden, 1999) or during subduction related to Sierra Nevada magmatism. Although the cause of the mantle enrichment in the Lassen (and Shasta) region is unclear, the data suggests that this component is distinct from the modern subduction component (Fig. 4). Therefore, in subsequent models and interpretations, we consider the enriched mantle as a single component and focus on the modern, volatile-rich and unradiogenic subduction component that is evident in the Lassen-region mafic magmas.

5.3 Evidence for slab melting

369 In the North Cascades, basaltic magma compositions can be explained by
370 three component mixing between DMM, sediment melts, and oceanic crust melts
371 (Fig. 4a; Mullen and Weis, 2015). However, the low Sr/Nd magmas in the Lassen
372 region cannot be explained by mixing of the same components, and the strong
373 negative correlation of the Lassen data (Fig. 4a) suggests the magmas are dominated
374 by two components – enriched sub-arc mantle and subducted MORB crust – with a
375 lesser role for sediment melt (Fig. 4b). These observations suggest that low-Sr/Nd
376 magmas in the Lassen region reflect their derivation from a sub-arc mantle with an
377 isotopically-enriched character, as explained in the previous section. New
378 radiogenic isotope data from this study overlap with previously published data (Fig.
379 4). Because elevated H_2O/Ce, Cl/Nb, and Sr/Nd ratios are related to subduction
380 component addition, our data confirm that the subduction component has a MORB-
381 like isotopic composition, with less radiogenic Sr and Pb than the Lassen sub-arc
382 mantle. In its isotopic characteristics, the subduction component is similar to
383 offshore Gorda Ridge MORB (Davis et al., 2008).
384 Melting of subducted MORB crust was discounted by Borg et al. (1997)
385 because melting of dry eclogitized oceanic lithosphere requires higher temperatures
386 than expected for the slab top at sub-arc depths. Grove et al. (2002) discounted slab
387 melting beneath Shasta, where similar isotopic relationships are observed (Fig. 4),
388 because models of hydrous peridotite melting could reproduce the observed major
389 element compositions of primitive volcanic rocks in that region. Recent work by
390 Walowski et al. (2015) interpreted the light D/H values of MI from the Lassen region
391 as resulting from final dehydration of chlorite in the hydrated upper mantle portion

392 of the downgoing slab. This provides a mechanism to deliver H_2O to the basaltic slab
393 top and drive wet slab melting beneath the arc, as proposed by Till et al. (2013),
394 Kimura et al. (2014), and Spandler and Pirard (2014).
395 To test this hypothesis, we calculated mixing and partial melting models
396 involving sub-arc mantle and a partial melt of Gorda MORB (Fig 4b, c). Because
397 temperatures of the plate top are at or above the wet MORB and wet sediment solidi
398 (Schmidt and Poli, 1998; Herman and Spandler, 2006), we assume the subduction
399 components are partial melts rather than aqueous fluids (Cooper et al., 2012;
400 Ruscitto et al., 2012; Kimura et al., 2014; Walowski et al., 2015). Our use of
401 unaltered Gorda MORB as the dominant slab component requires that the most
402 altered part of the slab (which contain seawater-derived Sr) loses much of its Sr
403 during dehydration beneath the forearc during transition to eclogite (Walowski et
404 al., 2015). Because Sr/Nd is an indicator of subduction enrichment, primitive basalts
405 with the lowest Sr/Nd values should be most representative of the Lassen sub-arc
406 mantle. These samples exhibit a small range of Sr, Nd, and Pb isotope ratios which is
407 probably indicative of mantle heterogeneity beneath the arc (Borg et al., 1997;
408 2002). We thus use a range in sub-arc mantle compositions (Fig. 4; $^{87}Sr/^{86}Sr$ =
409 0.7039 – 0.7043 and $^{208}Pb/^{204}Pb$ = 38.512 – 38.782). Figure 4b and c show curves
410 that represent melts of sub-arc mantle after addition of variable amounts of Gorda
411 MORB melt, the results of which suggest 1-10 wt% addition of the slab melt.
412 Our proposed mechanism for slab melting relies on breakdown of chlorite in
413 the lithospheric mantle of the downgoing plate. However, in the model shown in
414 Figure 4b and c, the chemical composition of this chlorite-derived fluid component

has been neglected. Fluids from the breakdown of chlorite at sub-arc depths have some distinct trace element characteristics (e.g., elevated LREE/HREE) but, overall, are solute poor (Spandler et al., 2014). As a result, chlorite-derived fluids will have little effect on the trace element composition of the magmas formed by flux melting of the upper oceanic crust. We therefore conclude that fluids derived from chlorite breakdown in the hydrated mantle portion of the slab dominantly contribute H_2O to the system but do not impart a distinctive trace element signature.

5.4 The role of sediment melts and crustal assimilation

Although the model results in Figures 4b and 4c can explain a majority of the compositions, some values of Sr and Pb isotopes are above the model predictions. There are three possible explanations for these small offsets: 1) contributions from zones of altered MORB in the downgoing plate that partially retained their altered isotopic signature after complete dehydration, 2) involvement of small proportions of a sediment melt component (Borg et al., 1997; 2002), and/or 3) contamination by crustal material. To further distinguish sediment and slab melt contributions, we use Th/La as a discriminant because of the high Th concentrations in sediments relative to MORB and sub-arc mantle (Fig. 4d; Plank et al., 2005). The mixing model in Figure 4d shows that Th/La variations in primitive Lassen magmas can result from addition of <10% of a subduction component made up of variable proportions of sediment and MORB melts. At all but two cinder cones, MI trace element compositions suggest that the slab component is dominated by melts of basaltic oceanic crust and contains <30% sediment melt. Two cinder cones (BPB and CC)

438 have larger apparent contributions from sediment melts. Cinder Cone, in particular,
439 contains the highest Th/La values from our dataset. However, the bulk lava and
440 tephra at this cone contain abundant quartz xenocrysts and variably melted granitic
441 xenoliths, which are clear indications of crustal contamination. This sample was
442 therefore excluded from radiogenic isotope analyses. We also note that MI from the
443 Lassen region samples have lower Th/La values on average than many of the
444 published bulk rock analyses from this area (Fig. 4d; Borg et al., 1997, 2002). This
445 could be because MI are trapped at depth, before even minor crustal contamination
446 occurs. Previous workers in the Lassen region interpreted unradiogenic Os isotopic
447 compositions in the most primitive basalts and basaltic andesites as evidence for
448 minimal contamination by continental crust (Borg et al., 1997, 2000). However, very
449 high Th concentrations in the granitic basement rocks (Cecil et al., 2012) make it
450 possible for small amounts of contamination to increase Th/La ratios to make it
451 difficult to differentiate between sediment melt and contamination.
452
453 **5.5 Modeling slab melt addition and the Sr/Y adakite signature**
454 The studied Lassen magmas have basaltic major element compositions and
455 are not high-Mg andesites as might be expected for magmas derived by slab melting
456 (Kelemen et al., 2003). To test whether the major and trace element compositions of
457 these magmas can be reproduced by slab melt addition to the mantle wedge, we
458 used pMELTS (Ghiorso et al., 2002) to compare the effects of fluid vs. hydrous melt
459 addition (Eiler et al., 2000) to the wedge at temperatures and pressures expected
460 for the Lassen sub-arc mantle. We created the starting bulk compositions by adding

461 various amounts of either a dacitic slab melt (Klimm et al., 2008) or pure H_2O to a
462 primitive mantle composition (MM3; Baker and Stolper, 1994). The pMELTS
463 program was used to determine the phase equilibria of the bulk mixture from 900-
464 1400°C at a pressure of 1.5 GPa. These values are based on temperatures from
465 geodynamic model results for the Lassen region (Walowski et al., 2015), beginning
466 at the slab-wedge interface to ~100°C hotter than peak temperatures expected in
467 the wedge. See Supplementary Discussion S3 for further details.
468 Melt fractions for both the hydrous-melt-fluxed and fluid-fluxed peridotite
469 cases are nearly indistinguishable (Supplementary Fig. S3). This suggests that for a
470 given mantle composition, the amount of H_2O supplied to the mantle controls the
471 degree of melting irrespective of whether the H_2O is added as melt or fluid,
472 consistent with experiments of Mallik et al. (2015). Figure 6 shows the major
473 element compositions of partial melts resulting from various amounts of slab melt
474 and aqueous fluid addition to the mantle wedge. For small amounts of slab melt
475 addition (1-3 wt%), the major element compositions of resulting basaltic melts are
476 similar to those of the aqueous fluid addition case. This indicates that equilibrium
477 between partial melt and residual mantle largely controls the major element
478 composition of the final melt. Primary magma compositions calculated from the MI
479 data overlap with the pMELTS model results (Fig. 6), demonstrating that hydrous-
480 melt-fluxed melting of the mantle wedge is a viable explanation for the production
481 of these magmas.
482 One hallmark of slab melt is high Sr/Y caused by the presence of garnet,
483 which makes up a large proportion of eclogitized MORB in the subducted plate

484 (Defant and Drummond, 1990). Most Lassen magmas, however, do not have high
485 Sr/Y values compared with the global array of adakites (Fig 7). Using the mixed
486 mantle compositions and melt fractions from the pMELTS models, melting curves in
487 Figure 8b show that for small amounts of slab melt addition (1-10%), the Sr/Y ratio
488 is dampened due to addition of Y from the spinel peridotite mantle component. This
489 yields values that overlap with values measured in MI from all but one sample
490 (BRM) from the Lassen region (Fig. 8b). The results are consistent with calculations
491 by Kelemen (1993) showing that peridotite-melt reaction produces melts with
492 lower LREE/HREE than the initial slab melts. Our model results suggest that high
493 Sr/Y adakitic signatures are only retained in arc magmas if slab melt addition is >10
494 wt%. Larger proportions of slab melt addition are thus required to explain the high
495 Sr/Y value of sample BRM, consistent with estimates of ~10% slab melt addition
496 inferred from radiogenic isotopes (Fig. 4). The high-Mg andesites from the Lassen
497 (M. Clynne, unpub. data) and Shasta regions that have higher values of Sr/Y (~150;
498 Ruscitto et al., 2011) could therefore be produced by larger amounts of hydrous slab
499 melt addition to the mantle wedge.
500 Although most primitive Cascade arc magmas do not have particularly high
501 Sr/Y compared to adakites, they do have other characteristics that indicate melting
502 in the presence of garnet when compared to the global array of basaltic arc magmas.
503 For example, primitive magmas from warm-slab subduction zones (Cascades,
504 Mexico) display elevated LREE/HREE and MREE/HREE (e.g. La/Yb and Dy/Yb;
505 Walowski et al., 2015 and Turner et al., 2015, respectively) and coupled high
506 $^{176}Hf/^{177}Hf$ and $^{143}Nd/^{144}Nd$ with lower values of Lu/Hf (Cai et al., 2014) when

507 compared to arcs associated with older oceanic crust. These relationships
508 demonstrate that partial melts of subducted oceanic crust play an increasingly
509 important role in the formation of magmas in arcs associated with young oceanic
510 crust.
511
512 **6. Model for magma generation beneath the southern Cascade arc**
513 Our results suggest that southern Cascade magmas are produced by a multi-
514 stage process involving fluid-flux melting of the basaltic slab top (±lesser sediment)
515 and ascent of this hydrous melt into the mantle wedge. Figure 8 shows a schematic
516 interpretation of this process based on the thermo-petrologic model results of
517 Walowski et al. (2015), the shear wave velocity model from Liu et al. (2012), and the
518 magnetotelluric data from Wannamaker et al. (2014). In our model, H_2O is retained
519 in the hydrated upper mantle portion of the downgoing slab to greater depths than
520 those at which H_2O is lost from the slab top (Fig. 9). Final chlorite breakdown occurs
521 in the slab interior when the slab top reaches ~75-80 km. At this depth, the upper
522 portions of the slab are above the MORB+H_2O solidus, and thus should melt when
523 fluxed by rising chlorite-derived fluids (e.g., Spandler and Pirard, 2013). The
524 resulting hydrous dacitic melts (Klimm et al., 2008) then rise into the overlying
525 mantle wedge and react with the surrounding mantle to produce hydrous, calc-
526 alkaline, basaltic to basaltic andesite melts (Fig. 7).
527 As a further test of this model, we determined whether breakdown of
528 chlorite can supply enough H_2O to balance the flux of H_2O from Cascade arc
529 magmatism. Previous work in Nicaragua (Ranero et al., 2003) and other arcs has

530 provided evidence for hydration of the deep slab and the importance of fluids
531 released from the deep slab in the production of arc magmas (e.g., Spandler and
532 Pirard, 2013). For the Juan de Fuca plate, higher temperatures at Moho depths
533 caused by the younger slab age may limit the extent of serpentinization (Nedimovic
534 et al., 2009), but no data are available for the Gorda plate to assess upper mantle
535 hydration. Due to this uncertainty, Walowski et al. (2015) conservatively assumed 2
536 km of hydration below the Moho of the downgoing plate and a bulk H_2O
537 concentration of 2 wt% for the hydrated peridotite. Using these model parameters,
538 the H_2O flux contributed by chlorite breakdown in the slab interior is estimated to
539 be ~1-2 x 10^6 kg/km arc length/yr. For the magmatic flux of H_2O from the Cascades,
540 we use the estimate from Ruscitto et al. (2012). This method, which includes
541 extrusive and intrusive magma fluxes and utilizes volatile contents from the central
542 Oregon Cascades (which overlap with those from the Lassen region), yields a
543 maximum H_2O flux of 1.93 x 10^6 kg/km/yr. This estimate agrees very well with the
544 flux from the thermo-petrologic model, demonstrating that fluids derived from the
545 breakdown of chlorite in the hydrated upper mantle portion of the slab may be
546 sufficient to produce observed volatile fluxes in the Cascade arc.
547 The thermo-petrologic model results of Walowski et al. (2015) predict two
548 main pulses of fluid from the downgoing slab associated with 1) the final
549 breakdown of hydrous phases during eclogitization of the oceanic crust, and 2) the
550 final breakdown of chlorite in the hydrated mantle portion of the slab (Fig. 9). The
551 first, more shallow pulse of fluid release correlates well with the location of a low-
552 resistivity anomaly beneath the forearc (Wannamaker et al., 2014), and likely

553 reflects a region of serpentinization of the cold nose of the mantle wedge. The
554 second, which causes flux melting of the slab top, agrees well with regions of low
555 shear wave velocity beneath the Lassen region (Liu et al., 2012). The shape of the
556 low shear wave velocity region is consistent with models of fluid migration into the
557 mantle wedge that suggest that for most values of wedge permeability, slab dip, and
558 convergence velocity there is a net migration of fluids and melts away from the
559 trench (Cagnioncle et al., 2007). This implies that arc magmas will inherit a slab
560 signature from a region of the slab that is slightly up-dip of the region that lies
561 directly beneath the arc. Therefore, patterns of decreasing amounts of a subduction
562 component towards the rear-arc, as observed in the geochemical data (Clynne,
563 1993; Borg et al., 1997; 2002), are consistent with the model in Figure 9.
564
565 **7. Conclusions**
566 The process of melt generation in warm-slab suduction zones, such as
567 Cascadia, has been debated due to the high slab surface temperatures and extensive
568 slab dehydration predicted by geodynamic and geochemical models. Our results
569 provide strong evidence that magma production in the southern Cascade arc is
570 driven by hydrous slab melt addition to the mantle wedge. Low B concentrations
571 and MORB-like B isotope ratios indicate that extensive dehydration of the plate
572 occurs before it reaches sub-arc depths. However, volatile concentrations and
573 correlations of volatile and trace element ratios (H_2O/Ce, Cl/Nb, Sr/Nd) show that
574 Lassen magmas have been enriched by variable amounts of addition of a hydrous
575 subduction component. Correlation of fluid mobile trace elements and radiogenic

isotopes demonstrates that the modern subduction component in the southern Cascades is less radiogenic than the sub-arc mantle wedge and must be dominantly derived from a partial melt of subducting Gorda MORB, with a minor contribution from subducted sediment melts. The pMELTS model results show that hydrous melt-fluxed melting of the mantle wedge can produce basaltic magmas with similar major element compositions to those measured in Lassen MI. Our results provide further evidence that chlorite-derived fluids from the deep slab interior can flux-melt the oceanic crust, producing hydrous slab melts that migrate into the overlying mantle, where they react with peridotite to induce further melting. The combined observations provide new insight on element recycling at subduction zones and demonstrate that partial melts of subducted oceanic crust play an important role in arcs associated with the subduction of young oceanic crust.

Acknowledgements

We thank Adam Kent for assistance with LA-ICP-MS measurements, Brian Monteleone for assistance with SIMS, John Donovan for assistance with EPMA, Erik Hauri for providing B-isotope standards, Nicole Marsh for carrying out the radiogenic isotope analyses at PCIGR, and Ilya Bindeman for their helpful comments. KJW thanks Angela Seligman, Ellen Aster, and Stan Mordensky for assistance in the field. We appreciate the constructive reviews of Catharine Chauvel, Maxim Portnyagin, and Dawnika Blatter, and assistance from the editor, Tamsin Mather. Funding was provided by the National Science Foundation (EAR-1119224 and EAR-1019848).

599

600 **Figure Captions**

601 *Figure 1:* a) Regional map of the Northwestern United States showing major tectonic
602 boundaries. The Cascade volcanic arc is defined by the major peaks (black triangles).
603 Lassen Peak is highlighted with a red triangle. Black arrows show convergence
604 direction and are labeled with the convergence rate relative to North America. b)
605 Larger scale map of the Lassen region with locations of vents sampled in this study
606 (BRVB: Basalt of Round Valley Butte; BPB: Basalt of Poison Butte; BRM: Basalt of
607 Red Mountain; BBL: Basalt of Big Lake; BAS-44: Basalt of Hwy 44; BPPC: Basalt of
608 Paine Parasitic Cone; BORG: Basalt of Old Railroad Grade; CC: Cinder Cone; see Table
609 1 for details) and previously sampled by Clynne (1993) and Borg (1995; gray
610 diamonds). Lassen Peak (large white triangle), outcropping basement rocks (shaded
611 pink areas), major highways (thin black lines), and large lakes (shaded blue regions),
612 are also highlighted. Distance from the trench vs. c) Sr/Nd and d) $^{87}Sr/^{86}Sr$ for
613 samples in this study (colored symbols) and Borg et al. (1997; gray diamonds).
614 Symbols and colors for individual cinder cones are consistent throughout the
615 manuscript.

616

617 *Figure 2:* a) Average MI trace element composition for each cone normalized to
618 normal-MORB (N-MORB; Sun and McDonough, 1989). Shown for comparison are
619 endmember compositions (CAB, Borg et al., 1997; HAOT, Bacon et al. 1997). b) K_2O
620 and SiO_2 contents of individual MI (corrected to equilibrium with host olivine and,

normalized on a volatile-free basis) compared with bulk rock analyses from Clynne (1993; gray diamonds).

Figure 3: Boron isotope compositions of Lassen MI. Each data point (symbols as in Fig. 1) represents an average of 4-8 individual MI from a given cone. Symbol size represents ≥1 SE (Table 2). Shown for comparison are data from the southern Washington Cascades (Leeman et al., 2004; filled squares, whole-rock analyses) Mt. Shasta (Rose et al., 2001, open circles; individual MI; LeVoyer et al., 2010, filled circles, MI), the Marianas (Ishikawa, 2001), and Kamchatka (Ishikawa and Tera, 1999). Dashed black curve represents basaltic magmas formed by flux melting of depleted MORB mantle by hydrous slab fluid (Marschall, 2007).

Figure 4: Bulk tephra isotopic compositions and average trace element compositions from MI (Table 2; filled symbols as in Figure 3;) and bulk tephra (open symbols; Walowski et al., 2015; no bulk tephra data available for BRM [purple]). a) $^{87}Sr/^{86}Sr$ vs. Sr/Nd; the North Cascades (pink shaded region in panel a; Mullen and Weis, 2015), and Mt. Adams (red shaded region in panel a; Jicha et al., 2009) are shown for comparison. Dashed lines connect the three components most likely to contribute to magma formation, as described in previous work (Mullen and Weis, 2015), but are not mixing models. Compositional similarity of bulk tephra and MI is described in Supplementary Discussion S2 and Fig. S2, which provides support for plotting MI compositions with bulk tephra radiogenic isotopes. Isotopic composition of BRM is from Borg et al. (1997), not this study. CC was omitted due to evidence for crustal

644 contamination (see text). Bulk lava analyses from the Lassen and Shasta regions
645 (Borg et al., 1997; Grove et al., 2002, respectively). b) Again, $^{87}Sr/^{86}Sr$ vs. Sr/Nd;
646 symbols as in a), now with North Cascade sediment (yellow shaded region;
647 Carpentier et al., 2013, 2014) and northern Sierran granites (gray shaded region;
648 Cecil et al., 2012) highlighted to show components that may contribute to trace
649 element and radiogenic isotope variability of samples. Melting models (dashed
650 lines) calculated using the batch melting equation for a range in mantle sources
651 (calculated for the Lassen sub-arc mantle; see Discussion section 5.2 for details)
652 mixed with 2, 5, and 10 wt.% (labeled on modeled curves) of a slab melt derived by
653 5% partial melting of Gorda MORB (Davis et al., 2008; partition coefficients [4 GPa,
654 1000°C] from Kessel et al., 2005a; Supplementary Table S6). Bulk partition
655 coefficients for mantle melting were calculated for a spinel peridotite assemblage
656 53/30/12/5-Ol/Opx/Cpx/Sp (Ruscitto et al., 2010) using partition coefficients of
657 Eiler et al. (2005) for Sr and Nd (Supplementary Table S6). Melt fractions were
658 derived from pMELTS model results (for a given temperature and amount of slab
659 melt addition; Fig. 6). c) $^{208}Pb/^{204}Pb$ vs. Sr/Nd; symbols and shaded regions as in
660 a,b), and mixing/melting model as in b). d) MI data only (from this study), and
661 Lassen bulk lava compositions from Borg et al. (1997). Curves represent partial
662 melting models for the Lassen sub-arc mantle (composition inferred from bulk rock
663 samples with smallest amount of apparent subduction component; see Discussion
664 section 5.2) mixed with either sediment partial melts (upper curves) or partial melts
665 from the basaltic slab (lower curves). The sediment partial melts were assumed to
666 be generated by either 5% partial melting (large filled gray diamond) or 20% partial

667 melting (small filled gray diamond) of N. Cascade sediment (partition coefficients
668 from Kessel et al., 2005a; Supplementary Table S6). The basaltic slab partial melts
669 likewise were assumed to be generated by either 5% partial melting (large filled
670 black diamond) or 20% partial melting (small filled black diamond) of Gorda MORB
671 (partition coefficients from Kessel et al., 2005a; Supplementary Table S6). The gray
672 shaded regions show the range of melt compositions created in the mantle by
673 addition of <10 wt% total of these subduction components (made with various
674 proportions of MORB vs. sediment melts) to the mantle wedge. The lines with tick
675 marks (in 10% increments) connecting the mixing curves are labeled with the
676 proportion of the subduction component derived from sediment partial melt, with
677 the remainder of the subduction component derived from the slab melt.
678
679 *Figure 5:* a) H_2O/Ce vs. Sr/Nd in MI. Data points are shown for MI that contain H_2O
680 concentrations within 0.5 wt% of the H_2O_{max} value for each cone, as these values
681 represent the least degassed compositions. b) Cl/Nb vs. Sr/Nd (all MI; corrected)
682 and c) Cl/Nb vs. Sr/Nd (average MI values for each cone; y-axis is extended to higher
683 values than in panel b). In a and c, data from central Oregon (Ruscitto et al., 2010;
684 solid blue circles enclosed in light blue shaded field] and Mt. Shasta (Ruscitto et al.,
685 2008; primitive basaltic andesite (PBA): solid gray triangles enclosed in gray shaded
686 field; high-Mg andesites (HMA): open gray triangles enclosed in a gray shaded field)
687 are shown for comparison. Black lines represent 10% partial melts of two
688 endmember mantle compositions (DMM; Workman and Hart, 2005; and average
689 central Oregon mantle; Ruscitto et al., 2010) mixed with variable amounts of a

690 hydrous subduction component (gray diamond in a; calculated using methods of
691 Portnyagin et al., 2007, based on primary magma composition of sample BORG;
692 Table 1). The gray bar represents the range in sub-arc mantle compositions
693 determined by Walowski et al. (2015). MI that experienced degassing before
694 entrapment or post-entrapment H loss will deviate from the melting curves as
695 indicated by the black arrow in panel a.
696
697 *Figure 6:* pMELTS model results compared with calculated primary magma
698 compositions from each cone (Table 1). a) H_2O, b) K_2O + Na_2O, c) CaO and d) Al_2O_3
699 wt% vs. SiO_2 (all major elements are normalized volatile free). Phase equilibria were
700 calculated using pMELTS with a starting bulk composition of a mantle source (MM3;
701 Baker and Stolper, 1994) mixed with 1, 2, 5, or 10% of either pure H_2O (dashed
702 curves) or a hydrous dacite melt (solid curves; dacite melt from Klimm et al., 2008)
703 at 1.5 GPa. Each curve represents melting model results from 900-1400°C, with
704 major element compositions normalized volatile free. See Supplementary
705 Discussion S3 and Supplementary Table S6 for model parameters and further
706 details.
707
708 *Figure 7:* Average values of Sr/Y and Y for each cone (Table 2) compared to global
709 range of adakite compositions (GEOROC database) and experimental partial melts of
710 eclogite (Klimm et al., 2008). Solid and dashed curves represent modeled mantle
711 melt compositions for various amounts of slab melt addition from 900-1350°C at 1.5
712 GPa. Modeled Sr and Y were calculated using the batch melting equation for a

713 mantle source (calculated for the Lassen sub-arc mantle) mixed with 2, 5, and 10%
714 (labeled on model curves) of a partial melt of Gorda MORB (as in Fig. 4d;
715 Supplementary Table S6). Bulk partition coefficients were calculated for a spinel
716 peridotite assemblage 35/30/12/5-Ol/Opx/Cpx/Sp using mineral partition
717 coefficients of Eiler et al. (2005) for Sr and Eiler et al. (2001) for Y (Supplementary
718 Table S6). Melt fractions were derived from pMELTS model results (for a given
719 temperature and amount of slab melt addition; Fig. S3).
720
721 *Figure 8:* Schematic diagram depicting the petrogenesis of Lassen region magmas.
722 Chlorite-derived fluids from the deep slab interior beneath the forearc vents (small
723 blue arrows) drive flux-melting of the oceanic crust (red colored area), producing
724 hydrous slab melts that migrate into the overlying mantle (red arrows), where they
725 react with peridotite to induce further melting. The location of hydrous phase
726 stability in the downgoing slab (dark blue shaded region) and main pulses of fluid
727 release from the slab (small light blue arrows) are based on the thermo-petrologic
728 model results of Walowski et al. (2015). Area of low-velocity (dark and light orange
729 shaded regions for latitudes 41° and 40.6° of the 2D models, respectively) based on
730 shear wave velocity model of Lui et al. (2012). Green shaded region shows the
731 location of low resistivity from Wannamaker et al. (2014).
732
733
734 **References**
735

736 Bacon, C. R., Bruggman, P. E., Christiansen, R. L., Clynne, M. A., Donnelly-Nolan, J. M.,
737 & Hildreth, W. (1997). Primitive magmas at five Cascades volcanic fields: melts from
738 hot, heterogeneous sub-arc mantle. *Canadian Mineralogist*, 35, 397-424.
739
740 Baker, M. B., & Stolper, E. M. (1994). Determining the composition of high-pressure
741 mantle melts using diamond aggregates. *Geochimica et Cosmochimica Acta*, 58(13),
742 2811-2827.
743
744 Behn, M. D., Kelemen, P. B., Hirth, G., Hacker, B. R., & Massonne, H. J. (2011). Diapirs
745 as the source of the sediment signature in arc lavas. *Nature Geoscience*, 4(9), 641-
746 646.
747
748 Berge, P. A., & Stauber, D. A. (1987). Seismic refraction study of upper crustal
749 structure in the Lassen Peak Area, northern California. *Journal of Geophysical*
750 *Research: Solid Earth* (1978–2012), 92(B10), 10571-10579.
751
752 Borg, L. E., Clynne, M. A., & Bullen, T. D. (1997). The variable role of slab-derived
753 fluids in the generation of a suite of primitive calc-alkaline lavas from the
754 southernmost Cascades, California. *Canadian Mineralogist*, 35, 425-452.
755
756 Borg, L. E., Brandon, A. D., Clynne, M. A., & Walker, R. J. (2000). Re–Os isotopic
757 systematics of primitive lavas from the Lassen region of the Cascade arc, California.
758 *Earth and Planetary Science Letters*, 177(3), 301-317.

736 Bacon, C. R., Bruggman, P. E., Christiansen, R. L., Clynne, M. A., Donnelly-Nolan, J. M.,
737 & Hildreth, W. (1997). Primitive magmas at five Cascades volcanic fields: melts from
738 hot, heterogeneous sub-arc mantle. *Canadian Mineralogist*, 35, 397-424.
739
740 Baker, M. B., & Stolper, E. M. (1994). Determining the composition of high-pressure
741 mantle melts using diamond aggregates. *Geochimica et Cosmochimica Acta*, 58(13),
742 2811-2827.
743
744 Behn, M. D., Kelemen, P. B., Hirth, G., Hacker, B. R., & Massonne, H. J. (2011). Diapirs
745 as the source of the sediment signature in arc lavas. *Nature Geoscience*, 4(9), 641-
746 646.
747
748 Berge, P. A., & Stauber, D. A. (1987). Seismic refraction study of upper crustal
749 structure in the Lassen Peak Area, northern California. *Journal of Geophysical*
750 *Research: Solid Earth* (1978–2012), 92(B10), 10571-10579.
751
752 Borg, L. E., Clynne, M. A., & Bullen, T. D. (1997). The variable role of slab-derived
753 fluids in the generation of a suite of primitive calc-alkaline lavas from the
754 southernmost Cascades, California. *Canadian Mineralogist*, 35, 425-452.
755
756 Borg, L. E., Brandon, A. D., Clynne, M. A., & Walker, R. J. (2000). Re–Os isotopic
757 systematics of primitive lavas from the Lassen region of the Cascade arc, California.
758 *Earth and Planetary Science Letters*, 177(3), 301-317.

782 Carpentier, M., Weis, D., & Chauvel, C. (2013). Large U loss during weathering of
783 upper crust: the sedimentary record. *Chemical Geology*, 340, 91-104.
784
785 Carpentier, M., Weis, D., & Chauvel, C. (2014). Fractionation of Sr and Hf isotopes by
786 mineral sorting in Cascadia Basin terrigenous sediments. *Chemical Geology*, 382, 67-
787 82.
788
789 Cecil, M. R., Rotberg, G. L., Ducea, M. N., Saleeby, J. B., & Gehrels, G. E. (2012).
790 Magmatic growth and batholithic root development in the northern Sierra Nevada,
791 California. *Geosphere*, 8(3), 592-606.
792
793 Clynne, M. A. (1993). Geologic studies of the Lassen volcanic center, Cascade Range,
794 California. University of California, Santa Cruz. Ph.D. Dissertation.
795
796 Clynne, M. A., & Muffler, L. J. P. (2010). Geologic map of Lassen Volcanic National
797 Park and vicinity, California. Scientific Investigations Map SIM-2899, US Geological
798 Survey.
799
800 Cooper, L. B., Ruscitto, D. M., Plank, T., Wallace, P. J., Syracuse, E. M., & Manning, C. E.
801 (2012). Global variations in H_2O/Ce: 1. Slab surface temperatures beneath volcanic
802 arcs. *GeocheMItry, Geophysics, Geosystems*, 13(3).
803

804 Danyushevsky, L. V., Sokolov, S., & Falloon, T. J. (2002). Melt inclusions in olivine
805 phenocrysts: using diffusive re-equilibration to determine the cooling history of a
806 crystal, with implications for the origin of olivine-phyric volcanic rocks. *Journal of*
807 *Petrology*, 43(9), 1651-1671.
808
809 Danyushevsky, L. V., & Plechov, P. (2011). Petrolog3: Integrated software for
810 modeling crystallization processes. *GeocheMItry, Geophysics, Geosystems*, 12(7).
811
812 Davis, A. S., Clague, D. A., Cousens, B. L., Keaten, R., & Paduan, J. B. (2008).
813 GeocheMItry of basalt from the North Gorda segment of the Gorda Ridge: Evolution
814 toward ultraslow spreading ridge lavas due to decreasing magma supply.
815 *GeocheMItry, Geophysics, Geosystems*, 9(4).
816
817 Defant, M. J., & Drummond, M. S. (1990). Derivation of some modern arc magmas by
818 melting of young subducted lithosphere. *Nature*, 347(6294), 662-665.
819
820 Eiler, J. M., Crawford, A., Elliott, T., Farley, K. A., Valley, J. W., & Stolper, E. M. (2000).
821 Oxygen isotope geocheMItry of oceanic-arc lavas. *Journal of Petrology*, 41(2), 229-
822 256.
823
824 Eiler, J. M., Carr, M. J., Reagan, M., & Stolper, E. (2005). Oxygen isotope constraints on
825 the sources of Central American arc lavas. *GeocheMItry, Geophysics, Geosystems*, 6(7).
826

827 Ford, C. E., Russell, D. G., Craven, J. A., & Fisk, M. R. (1983). Olivine-liquid equilibria:
828 temperature, pressure and composition dependence of the crystal/liquid cation
829 partition coefficients for Mg, Fe2+, Ca and Mn. *Journal of Petrology*, 24(3), 256-266.
830
831 Gerya, T. V., & Yuen, D. A. (2003). Rayleigh–Taylor instabilities from hydration and
832 melting propel 'cold plumes' at subduction zones. *Earth and Planetary Science*
833 *Letters*, 212(1), 47-62.
834
835 Ghiorso, M. S., Hirschmann, M. M., Reiners, P. W., & Kress, V. C. (2002). The pMELTS:
836 A revision of MELTS for improved calculation of phase relations and major element
837 partitioning related to partial melting of the mantle to 3 GPa. *GeocheMItry,*
838 *Geophysics, Geosystems*, 3(5), 1-35.
839
840 Grove, T., Parman, S., Bowring, S., Price, R., & Baker, M. (2002). The role of an H_2O-
841 rich fluid component in the generation of primitive basaltic andesites and andesites
842 from the Mt. Shasta region, N. California. *Contributions to Mineralogy and Petrology*,
843 142(4), 375-396.
844
845 Guffanti, M., Clynne, M. A., Smith, J. G., Muffler, L. J. P., & Bullen, T. D. (1990). Late
846 Cenozoic volcanism, subduction, and extension in the Lassen region of California,
847 southern Cascade Range. *Journal of Geophysical Research*, 95(B12), 19453-19464.
848

Hermann, J., Spandler, C., Hack, A., & Korsakov, A. V. (2006). Aqueous fluids and hydrous melts in high-pressure and ultra-high pressure rocks: implications for element transfer in subduction zones. *Lithos*, 92(3), 399-417.

Hirschmann, M. M., Baker, M. B., & Stolper, E. M. (1998). The effect of alkalis on the silica content of mantle-derived melts. *Geochimica et Cosmochimica Acta*, 62(5), 883-902.

Irwin, W.P., & Wooden, J.L., 1999, Plutons and accretionary episodes of the Klamath Mountains, California and Oregon. U. S. Geological Survey, Open-file Report 99-374.

Ishikawa, T., & Nakamura, E. (1993). Boron isotope systematics of marine sediments. *Earth and Planetary Science Letters*, 117(3), 567-580.

Ishikawa, T., & Tera, F. (1999). Two isotopically distinct fluid components involved in the Mariana arc: Evidence from Nb/B ratios and B, Sr, Nd, and Pb isotope systematics. *Geology*, 27(1), 83-86.

Ishikawa, T., & Tera, F. (1999). Two isotopically distinct fluid components involved in the Mariana Arc: Evidence from Nb/B ratios and B, Sr, Nd, and Pb isotope systematics. *Geology*, 27(1), 83-86.

871 Ishikawa, T., Tera, F., & Nakazawa, T. (2001). Boron isotope and trace element
872 systematics of the three volcanic zones in the Kamchatka arc. *Geochimica et*
873 *Cosmochimica Acta*, 65(24), 4523-4537.
874
875 Jicha, B. R., Hart, G. L., Johnson, C. M., Hildreth, W., Beard, B. L., Shirey, S. B., & Valley, J.
876 W. (2009). Isotopic and trace element constraints on the petrogenesis of lavas from
877 the Mount Adams volcanic field, Washington. *Contributions to Mineralogy and*
878 *Petrology*, 157(2), 189-207.
879
880 Johnson, E. R., Wallace, P. J., Cashman, K. V., Granados, H. D., & Kent, A. J. (2008).
881 Magmatic volatile contents and degassing-induced crystallization at Volcán Jorullo,
882 Mexico: implications for melt evolution and the plumbing systems of monogenetic
883 volcanoes. *Earth and Planetary Science Letters*, 269(3), 478-487.
884
885 Johnson, E. R., Wallace, P. J., Granados, H. D., Manea, V. C., Kent, A. J., Bindeman, I. N.,
886 & Donegan, C. S. (2009). Subduction-related volatile recycling and magma
887 generation beneath Central Mexico: insights from melt inclusions, oxygen isotopes
888 and geodynamic models. *Journal of Petrology*, 50(9), 1729-1764.
889
890 Kelemen, P. B., Shimizu, N., & Dunn, T. (1993). Relative depletion of niobium in some
891 arc magmas and the continental crust: partitioning of K, Nb, La and Ce during
892 melt/rock reaction in the upper mantle. *Earth and Planetary Science Letters*, 120(3),
893 111-134.

894

895 Kelemen, P. B., Yogodzinski, G. M., & Scholl, D. W. (2003). Along-strike variation in
896 the Aleutian island arc: Genesis of high Mg# andesite and implications for
897 continental crust. *Inside the Subduction Factory, Geophys. Monogr. Ser*, 138, 223-276.
898
899 Kessel, R., Schmidt, M. W., Ulmer, P., & Pettke, T. (2005). Trace element signature of
900 subduction-zone fluids, melts and supercritical liquids at 120–180 km depth. *Nature*,
901 437(7059), 724-727.
902
903 Kimura, J. I., & Nakajima, J. (2014). Behaviour of subducted water and its role in
904 magma genesis in the NE Japan arc: A combined geophysical and geochemical
905 approach. *Geochimica et Cosmochimica Acta*, 143, 165-188.
906
907 Klimm, K., Blundy, J. D., & Green, T. H. (2008). Trace element partitioning and
908 accessory phase saturation during H2O-saturated melting of basalt with
909 implications for subduction zone chemical fluxes. *Journal of Petrology*, 49(3), 523-
910 553.
911
912 Krawczynski, M. J., Grove, T. L., & Behrens, H. (2012). Amphibole stability in
913 primitive arc magmas: effects of temperature, H_2O content, and oxygen fugacity.
914 *Contributions to Mineralogy and Petrology*, 164(2), 317-339.
915

916 Leeman, W. P., Tonarini, S., Chan, L. H., & Borg, L. E. (2004). Boron and lithium
917 isotopic variations in a hot subduction zone—the southern Washington Cascades.
918 *Chemical Geology*, 212(1), 101-124.
919
920 Liu, K., Levander, A., Zhai, Y., Porritt, R. W., & Allen, R. M. (2012). Asthenospheric
921 flow and lithospheric evolution near the Mendocino Triple Junction. *Earth and*
922 *Planetary Science Letters*, 323, 60-71.
923
924 Lloyd, A. S., Plank, T., Ruprecht, P., Hauri, E. H., & Rose, W. (2013). Volatile loss from
925 melt inclusions in pyroclasts of differing sizes. *Contributions to Mineralogy and*
926 *Petrology*, 165(1), 129-153.
927
928 Loewen, M. W., & Kent, A. J. (2012). Sources of elemental fractionation and
929 uncertainty during the analysis of semi-volatile metals in silicate glasses using LA-
930 ICP-MS. *Journal of Analytical Atomic Spectrometry*, 27(9), 1502-1508.
931
932 Le Voyer, M., Rose-Koga, E. F., Shimizu, N., Grove, T. L., & Schiano, P. (2010). Two
933 contrasting H_2O-rich components in primary melt inclusions from Mount Shasta.
934 *Journal of Petrology*, 51(7), 1571-1595.
935
936 Mallik, A., Nelson, J., & Dasgupta, R. (2015). Partial melting of fertile peridotite fluxed
937 by hydrous rhyolitic melt at 2–3 GPa: implications for mantle wedge hybridization

by sediment melt and generation of ultrapotassic magmas in convergent margins. *Contributions to Mineralogy and Petrology*, 169(5), 1-24.

Manea, V. C., Leeman, W. P., Gerya, T., Manea, M., & Zhu, G. (2014). Subduction of fracture zones controls mantle melting and geochemical signature above slabs. *Nature Communications*, 5.

Marschall, H. R., & Monteleone, B. D. (2014). Boron isotope analysis of silicate glass with very low boron concentrations by Secondary Ion Mass Spectrometry. *Geostandards and Geoanalytical Research*. 39(1), 31-46.

Marschall, H. R., Altherr, R., & Rüpke, L. (2007). Squeezing out the slab—modelling the release of Li, Be and B during progressive high-pressure metamorphism. *Chemical Geology*, 239(3), 323-335.

Moore, L. R., Gazel, E., Tuohy, R., Lloyd, A. S., Esposito, R., Steele-MacInnis, M., & Bodnar, R. J. (2015). Bubbles matter: An assessment of the contribution of vapor bubbles to melt inclusion volatile budgets. *American Mineralogist*, 100(4), 806-823.

Mullen, E. K., & Weis, D. (2015). Evidence for trench-parallel mantle flow in the northern Cascade Arc from basalt geocheMItry. *Earth and Planetary Science Letters*, 414, 100-107.

961 Nedimović, M. R., Bohnenstiehl, D. R., Carbotte, S. M., Canales, J. P., & Dziak, R. P.
962 (2009). Faulting and hydration of the Juan de Fuca plate system. *Earth and Planetary*
963 *Science Letters*, 284(1), 94-102.
964
965 Mallmann, G., & O'Neill, H. S. C. (2009). The crystal/melt partitioning of V during
966 mantle melting as a function of oxygen fugacity compared with some other elements
967 (Al, P, Ca, Sc, Ti, Cr, Fe, Ga, Y, Zr and Nb). *Journal of Petrology*, 50(9), 1765-1794.
968
969 Plank, T. (2005). Constraints from thorium/lanthanum on sediment recycling at
970 subduction zones and the evolution of the continents. *Journal of Petrology*, 46(5),
971 921-944.
972
973 Plank, T., Kelley, K. A., Zimmer, M. M., Hauri, E. H., & Wallace, P. J. (2013). Why do
974 mafic arc magmas contain 4wt% water on average? *Earth and Planetary Science*
975 *Letters*, 364, 168-179.
976
977 Portnyagin, M., Hoernle, K., Plechov, P., Mironov, N., & Khubunaya, S. (2007).
978 Constraints on mantle melting and composition and nature of slab components in
979 volcanic arcs from volatiles (H_2O, S, Cl, F) and trace elements in melt inclusions from
980 the Kamchatka Arc. *Earth and Planetary Science Letters*, 255(1), 53-69.
981

982 Ranero, C. R., Morgan, J. P., McIntosh, K., & Reichert, C. (2003). Bending-related
983 faulting and mantle serpentinization at the Middle America trench. *Nature*,
984 425(6956), 367-373.
985
986 Rose, E. F., Shimizu, N., Layne, G. D., & Grove, T. L. (2001). Melt production beneath
987 Mt. Shasta from boron data in primitive melt inclusions. *Science*, 293(5528), 281-
988 283.
989
990 Ruscitto, D. M., Wallace, P. J., Johnson, E. R., Kent, A. J. R., & Bindeman, I. N. (2010).
991 Volatile contents of mafic magmas from cinder cones in the Central Oregon High
992 Cascades: 63. Implications for magma formation and mantle conditions in a hot arc.
993 *Earth and Planetary Science Letters*, 298(1), 153-161.
994
995 Ruscitto, D. M., Wallace, P. J., & Kent, A. J. R. (2011). Revisiting the compositions and
996 volatile contents of olivine-hosted melt inclusions from the Mount Shasta region:
997 implications for the formation of high-Mg andesites. *Contributions to Mineralogy and*
998 *Petrology*, 162(1), 109-132.
999
1000 Ruscitto, D. M., Wallace, P. J., Cooper, L. B., & Plank, T. (2012). Global variations in
1001 H2O/Ce: 2. Relationships to arc magma geocheMItry and volatile fluxes.
1002 *GeocheMItry, Geophysics, Geosystems*, 13(3).
1003

1004 Schmidt, M. W., & Poli, S. (1998). Experimentally based water budgets for
1005 dehydrating slabs and consequences for arc magma generation. *Earth and Planetary*
1006 *Science Letters*, 163(1), 361-379.
1007
1008 Spandler, C., & Pirard, C. (2013). Element recycling from subducting slabs to arc
1009 crust: a review. *Lithos*, 170, 208-223.
1010
1011 Spandler, C., Pettke, T., & Hermann, J. (2014). Experimental study of trace element
1012 release during ultrahigh-pressure serpentinite dehydration. *Earth and Planetary*
1013 *Science Letters*, 391, 296-306.
1014
1015 Sun, S. S., & McDonough, W. F. (1989). Chemical and isotopic systematics of oceanic
1016 basalts: implications for mantle composition and processes. *Geological Society,*
1017 *London, Special Publications*, 42(1), 313-345.
1018
1019 Syracuse, E. M., van Keken, P. E., & Abers, G. A. (2010). The global range of
1020 subduction zone thermal models. *Physics of the Earth and Planetary Interiors*, 183(1),
1021 73-90.
1022
1023 Till, C. B., Grove, T. L., Carlson, R. W., Donnelly-Nolan, J. M., Fouch, M. J., Wagner, L. S.,
1024 & Hart, W. K. (2013). Depths and temperatures of< 10.5 Ma mantle melting and the
1025 lithosphere-asthenosphere boundary below southern Oregon and northern
1026 California. *GeocheMItry, Geophysics, Geosystems*, 14(4), 864-879.

1027

1028 Tonarini, S., Armienti, P., D'Orazio, M., & Innocenti, F. (2001). Subduction-like fluids
1029 in the genesis of Mt. Etna magmas: evidence from boron isotopes and fluid mobile
1030 elements. *Earth and Planetary Science Letters*, 192(4), 471-483.

1031

1032 Turner, S. J., & C. H. Langmuir (2015). What processes control the chemical
1033 compositions of arc front stratovolcanoes? *GeocheMItry, Geophysics, Geosystems*. 16,
1034 1865–1893

1035

1036 Van Keken, P. E., Hacker, B. R., Syracuse, E. M., & Abers, G. A. (2011). Subduction
1037 factory: 4. Depth-dependent flux of H_2O from subducting slabs worldwide. *Journal of*
1038 *Geophysical Research: Solid Earth* (1978–2012), 116(B1).

1039

1040 Wada, I., & Wang, K. (2009). Common depth of slab-mantle decoupling: Reconciling
1041 diversity and uniformity of subduction zones. *GeocheMItry, Geophysics, Geosystems*,
1042 10(10).

1043

1044 Wallace, P. J., Kamenetsky, V. S., & Cervantes, P. (2015). Melt inclusion CO_2 contents,
1045 pressures of olivine crystallization, and the problem of shrinkage bubbles. *American*
1046 *Mineralogist*, 100(4), 787-794.

1047

1048 Walowski, K.J., Wallace P.J., Hauri, E.K., Wada, I., Clynne, M. A., (2015) Slab melting
1049 beneath the Cascade Arc driven by dehydration of altered oceanic peridotite. *Nature*
1050 *Geoscience*, 8(5), 404-408.
1051
1052 Wannamaker, P. E., Booker, J. R., Jones, A. G., Chave, A. D., Filloux, J. H., Waff, H. S., &
1053 Law, L. K. (1989). Resistivity cross section through the Juan de Fuca subduction
1054 system and its tectonic implications. *Journal of Geophysical Research: Solid Earth*
1055 (1978–2012), 94(B10), 14127-14144.
1056
1057
1058 Weis, D., Kieffer, B., Maerschalk, C., Barling, J., De Jong, J., Williams, G. A, & Mahoney, J.
1059 B. (2006). High-precision isotopic characterization of USGS reference materials by
1060 TIMS and MC-ICP-MS. *GeocheMItry, Geophysics, Geosystems*, 7(8).
1061
1062 Weis, D., Kieffer, B., Hanano, D., Nobre Silva, I., Barling, J., Pretorius, W. & Mattielli, N.
1063 (2007). Hf isotope compositions of US Geological Survey reference materials.
1064 *GeocheMItry, Geophysics, Geosystems*, 8(6).
1065
1066 Wilson, D. S. (2002). The Juan de Fuca plate and slab: Isochron structure and
1067 Cenozoic plate motions. US Geological Survey Open-File Report, 02-328.
1068
1069 Workman, R. K., & Hart, S. R. (2005). Major and trace element composition of the
1070 depleted MORB mantle (DMM). *Earth and Planetary Science Letters*, 231(1), 53-72.

Figure
Click here to download high resolution image

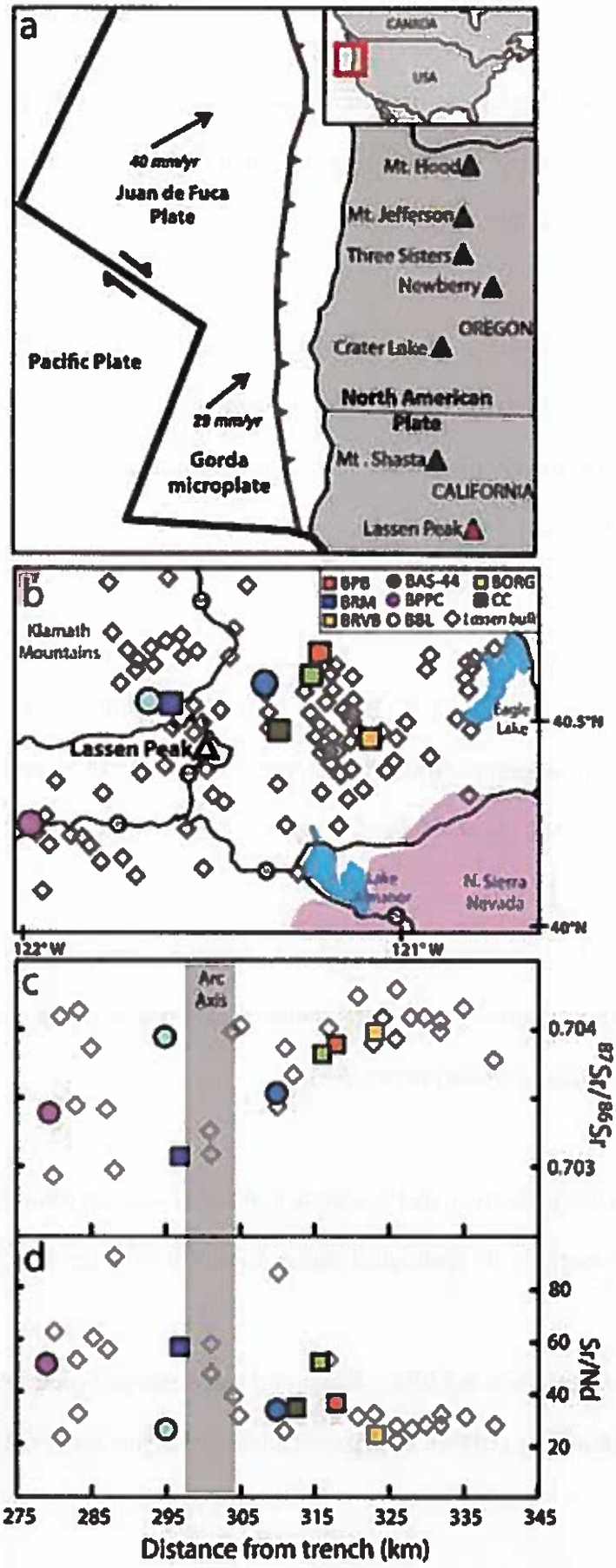

Figure
Click here to download high resolution image

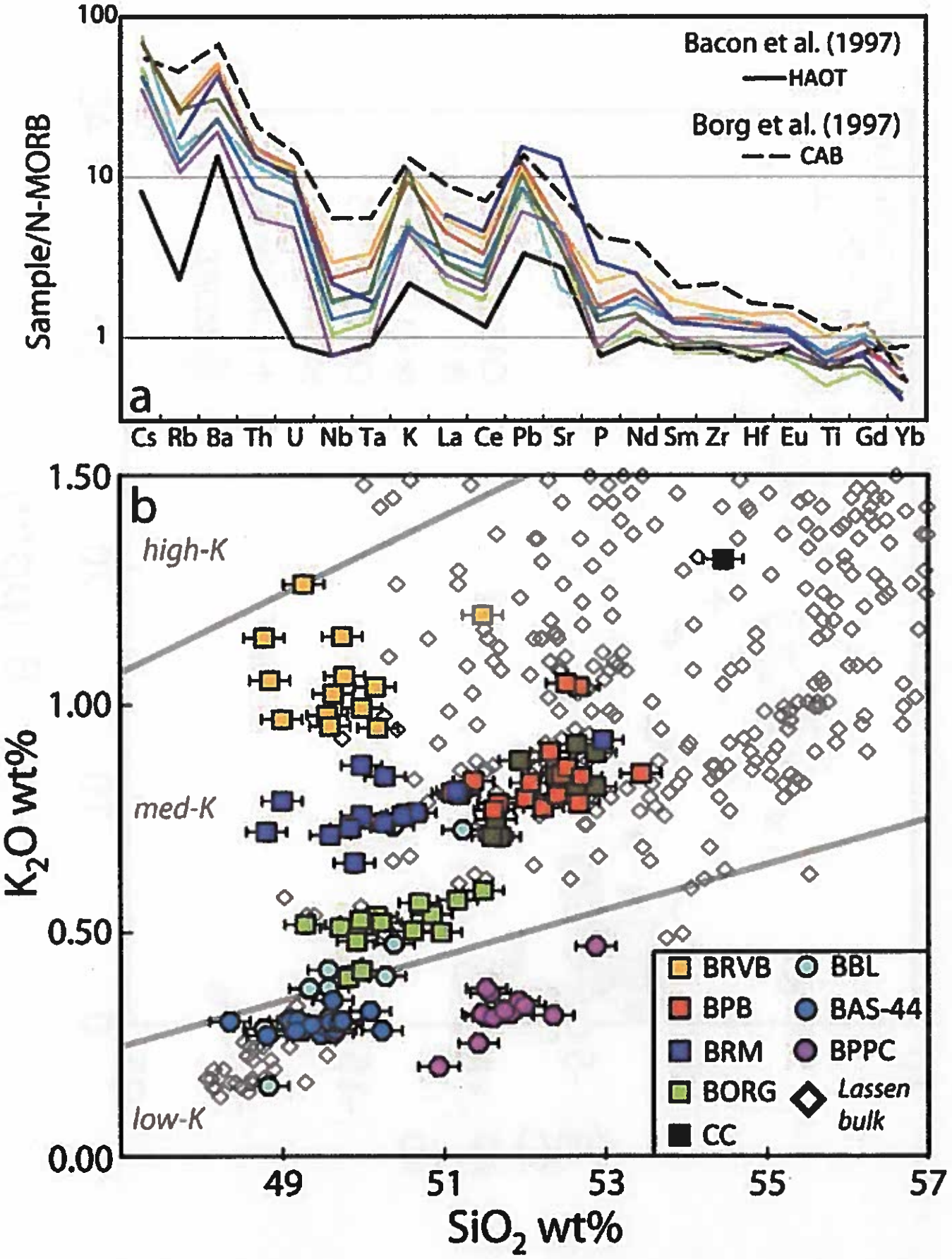

Figure
Click here to download high resolution image

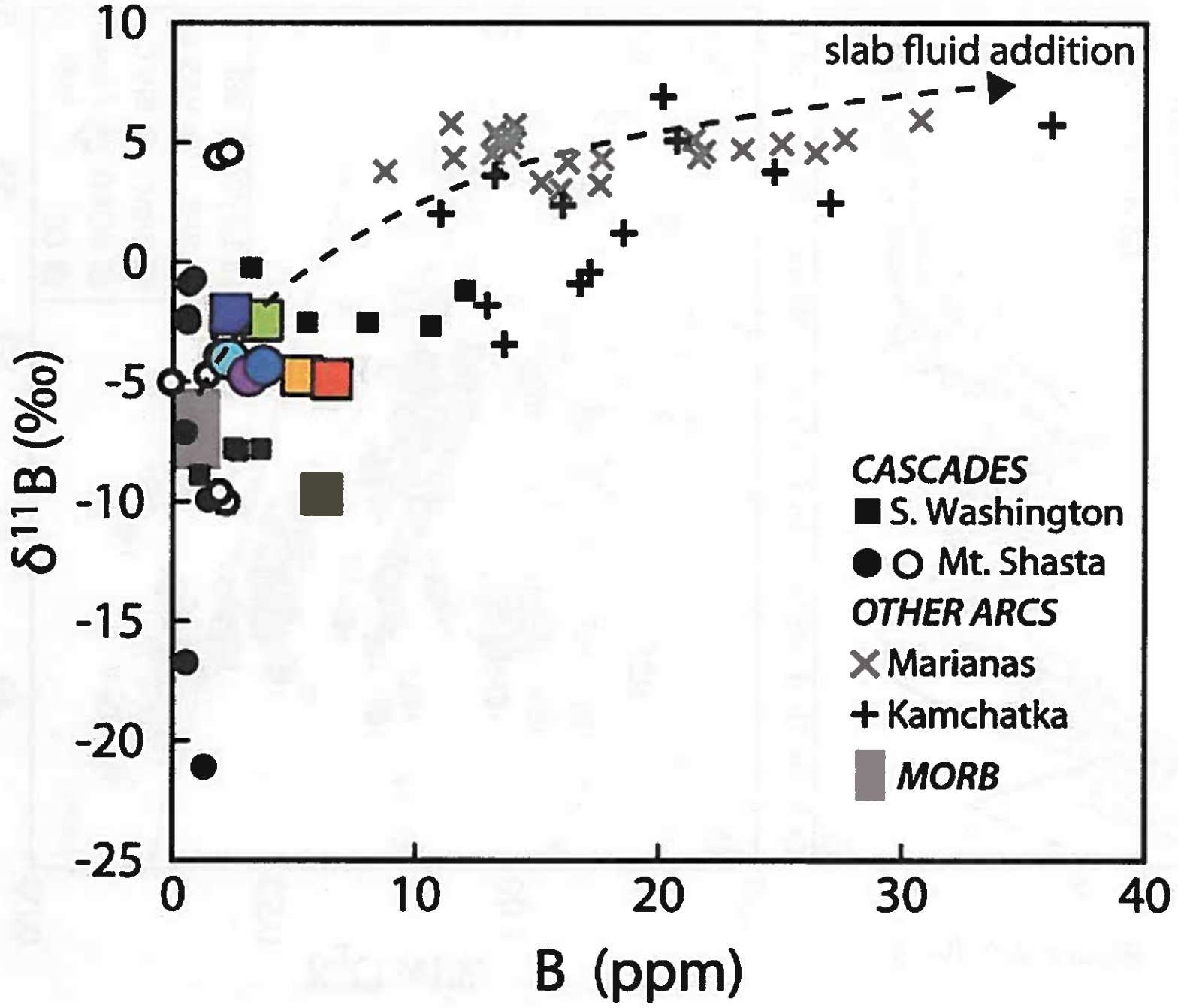

Figure
Click here to download high resolution image

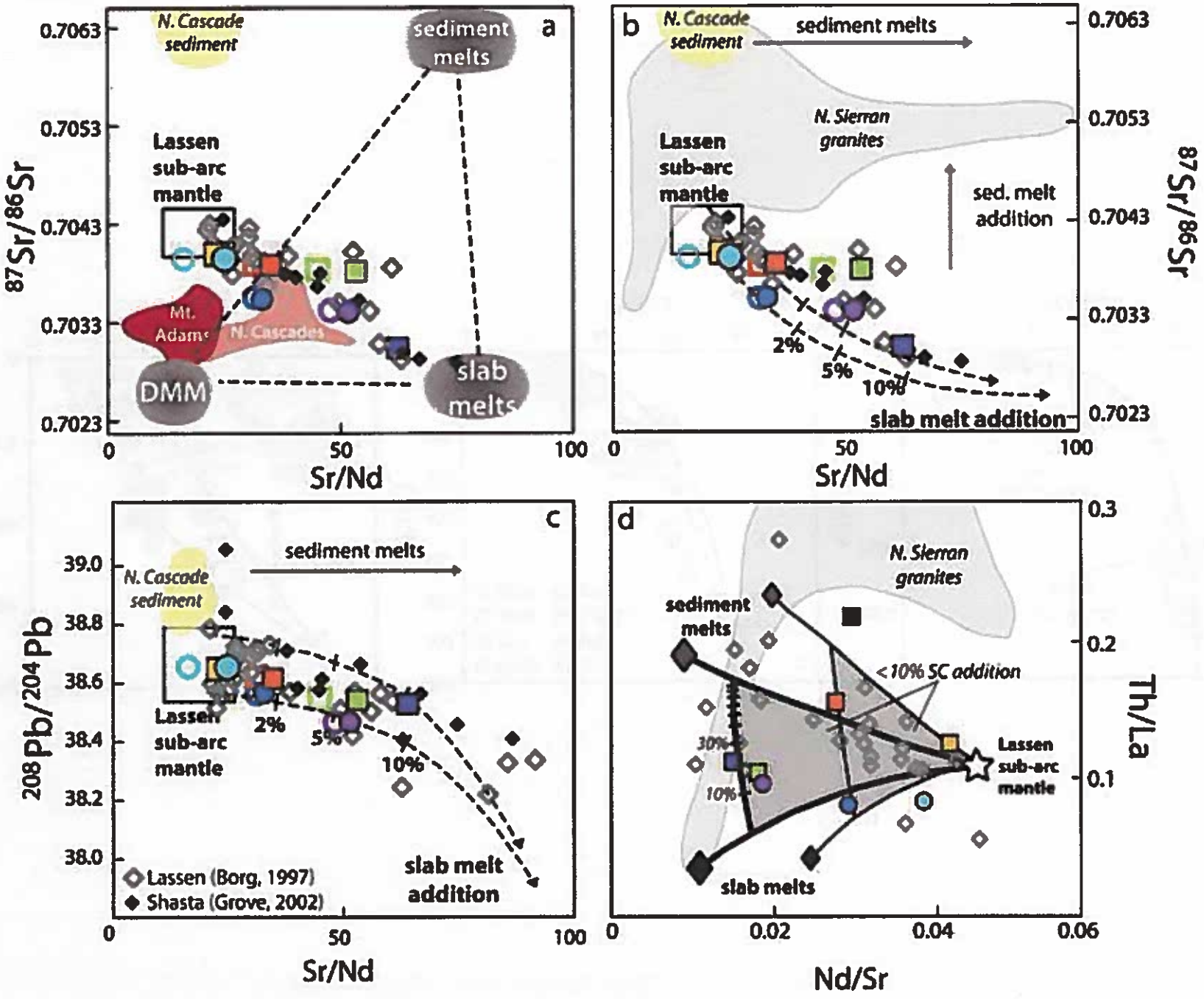

Figure
Click here to download high resolution image

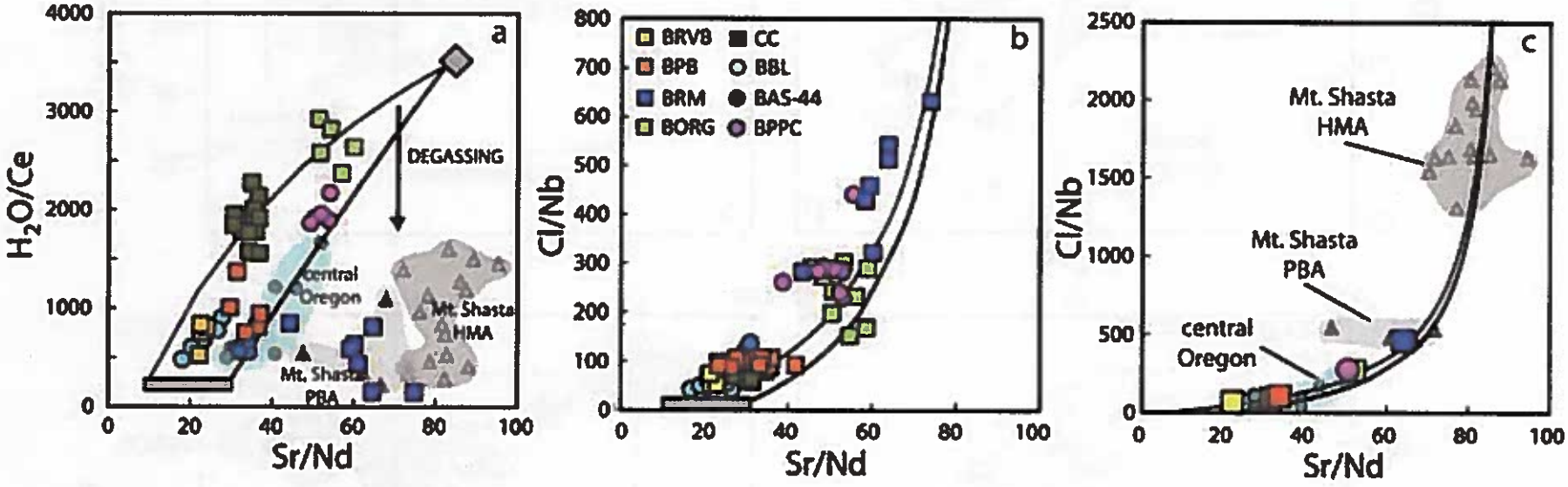

Figure
Click here to download high resolution image

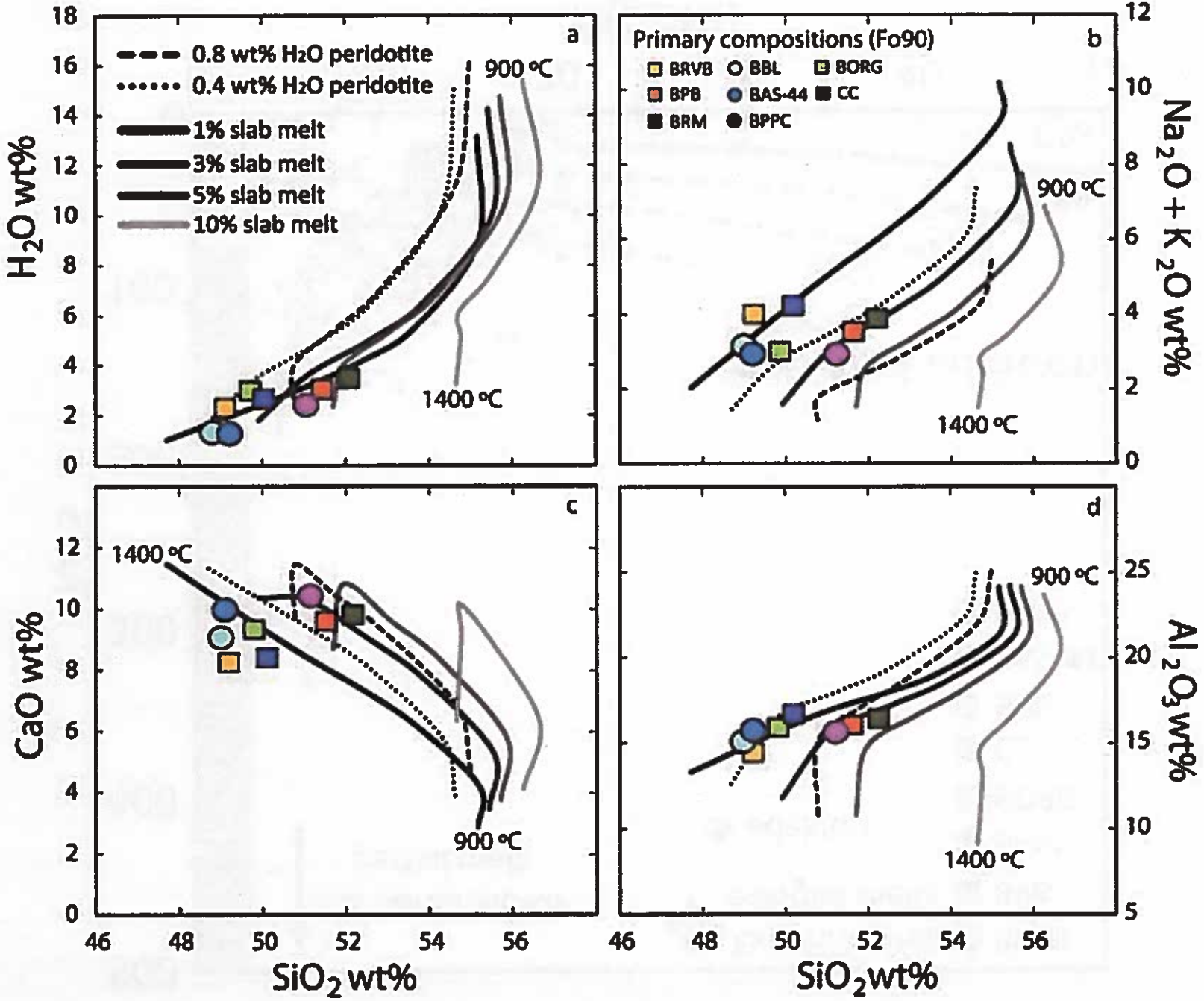

Figure
Click here to download high resolution image

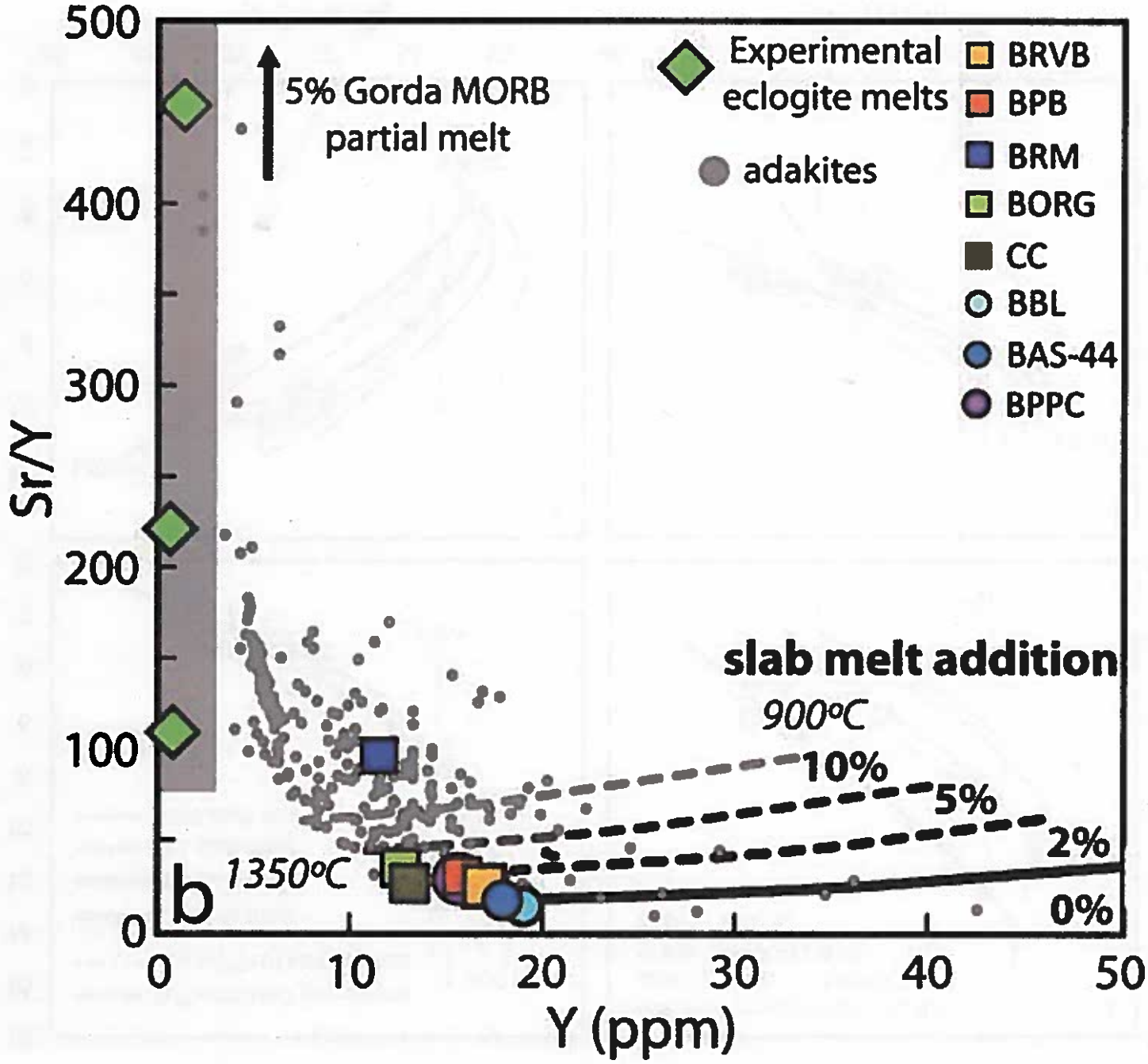

Figure
Click here to download high resolution image

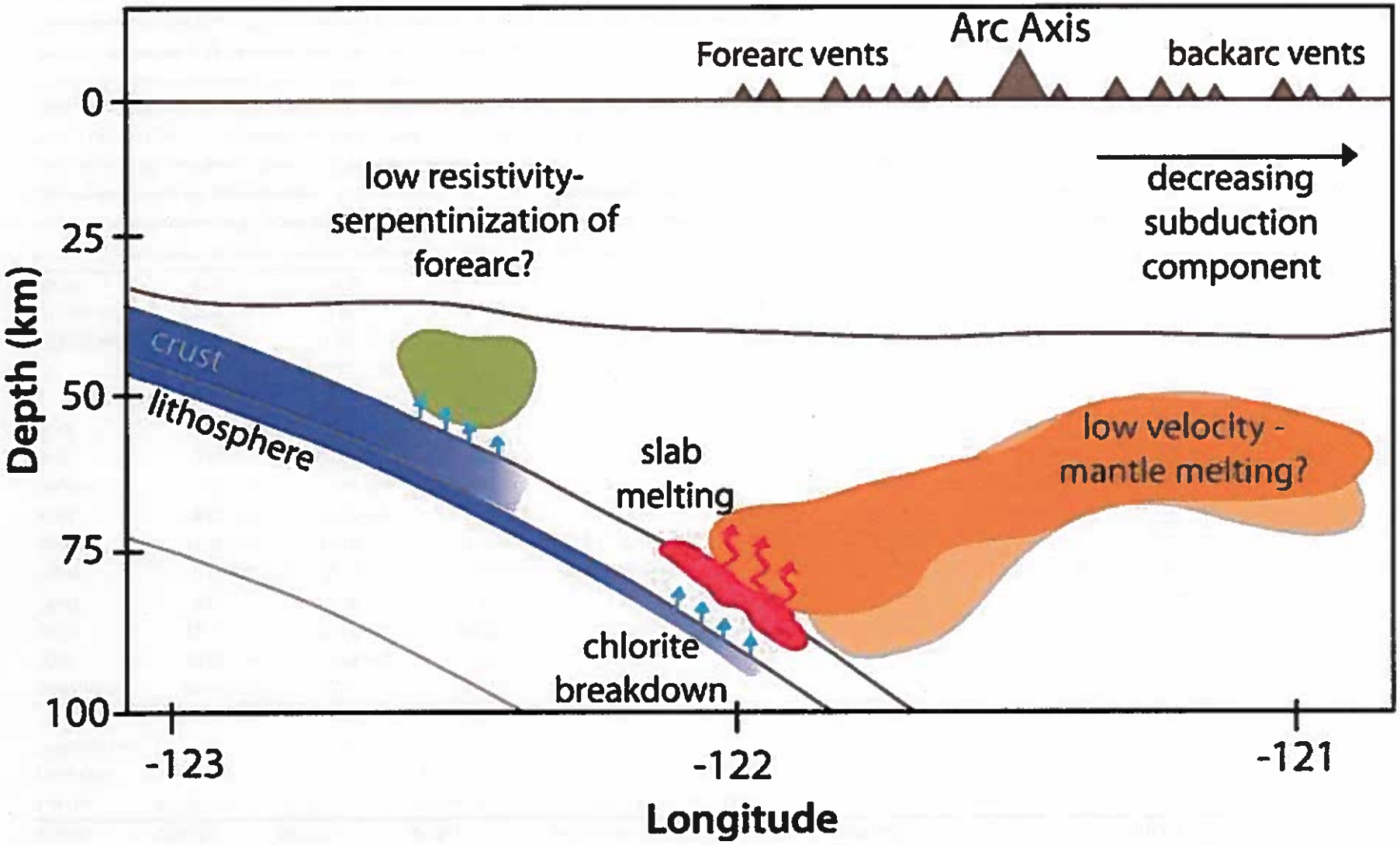

Table
Click here to download Table: Table 1.pdf

Table 1: Primary melt compositions (Major and Volatile)

Sample	BBL-05	BORG-1	BPB-1	BAS-44-02	BPPC-01	BRVB-01	CC-1	BRM-1
Lat (N)	40°34'33.72"	40°39'15.63"	40°40'40.80"	40°37'50.64"	40°19'34.22"	40°31'48.78"	40°32'24.50"	40°34'13.17"
Long (W)	121°37'1.32"	121°13'29.07"	121°12'51.00"	121°20'40.14"	121°54'38.64"	121° 4'34.32"	121°18'37.00"	121°35'31.59"
[a]Distance (km)	295	316	318	310	279	323	312	297
	n = 11 *1 s.d.*	n = 15	n = 16	n = 17	n = 14	n = 14	n = 13	n = 15
SiO_2 *(wt%)*	48.94 *0.22*	49.95 *0.14*	51.52 *0.26*	49.42 *0.33*	51.16 *0.12*	48.96 *0.20*	52.54 *0.15*	49.85 *0.11*
TiO_2	0.92 *0.04*	0.70 *0.01*	0.84 *0.01*	0.93 *0.07*	0.76 *0.02*	1.22 *0.01*	0.86 *0.02*	0.77 *0.00*
Al_2O_3	14.72 *0.15*	16.14 *0.16*	15.98 *0.33*	16.23 *0.29*	15.69 *0.11*	13.98 *0.12*	17.15 *0.25*	16.25 *0.11*
[b]FeO^T	9.10	8.18	7.23	8.22	7.38	9.24	5.93	8.06
MnO	0.12 *0.007*	0.10 *0.005*	0.11 *0.005*	0.12 *0.002*	0.12 *0.005*	0.11 *0.002*	0.09 *0.004*	0.09 *0.002*
MgO	14.01 *0.28*	12.40 *0.13*	11.00 *0.27*	11.50 *0.09*	11.18 *0.07*	14.30 *0.09*	8.85 *0.27*	12.41 *0.07*
CaO	8.82 *0.15*	9.33 *0.05*	9.53 *0.18*	10.28 *0.14*	10.51 *0.07*	7.96 *0.17*	10.31 *0.18*	8.12 *0.04*
Na_2O	2.72 *0.08*	2.50 *0.04*	2.67 *0.07*	2.68 *0.06*	2.60 *0.04*	2.91 *0.06*	3.15 *0.07*	3.40 *0.08*
P_2O_5	0.16 *0.05*	0.09 *0.02*	0.23 *0.02*	0.15 *0.05*	0.18 *0.02*	0.27 *0.04*	0.16 *0.01*	0.26 *0.00*
K_2O	0.36 *0.016*	0.47 *0.003*	0.78 *0.007*	0.28 *0.016*	0.30 *0.004*	0.93 *0.002*	0.85 *0.004*	0.68 *0.002*
S	0.09 *0.003*	0.11 *0.004*	0.09 *0.010*	0.11 *0.016*	0.11 *0.004*	0.13 *0.003*	0.09 *0.007*	0.16 *0.002*
Cl	0.02 *0.002*	0.05 *0.001*	0.05 *0.005*	0.03 *0.002*	0.04 *0.001*	0.04 *0.000*	0.04 *0.002*	0.20 *0.001*
[c]CO_2 *(ppm)*	884 *52*	1384 *111*	1436 *47*	754 *56*	1209 *72*	622 *118*	1436 *58*	521 *44*
[d]H_2O *(wt%)*	1.29 *0.08*	3.02 *0.15*	2.94 *0.22*	1.21 *0.22*	2.29 *0.14*	2.28 *0.10*	3.45 *0.10*	2.58 *0.03*
[e]% Ol	17.0	7.9	8.8	4.0	7.5	20.1	1.0	14.8

Primary melt compositions refer to the average MI composition calculated to be in equilibrium with Fo_{xx} olivine for each cone (further explanation in Methods).

Major element uncertainty calculated as one standard deviation of the population used to calculate the average MI composition from each cone (including analytical uncertainty)

The complete corrected and uncorrected dataset of MI compositions can be found in Supplementary Tables S1 and S4. Sample names are abbreviations based on Clynne and Muffler (2010):

BBL = Basalt of Big Lake; BORG = Basalt of Old Railroad Grade 3; BPB = Basalt of Poison Butte 3; BAS-44 = Basalt of Highway 44; and unpublished locations:

BPPC = Basalt of Paynes Creek Parasitic Cone; BRVB = Basalt of Round Valley Butte; BRM = Basalt of Red Mountain. Locations are based on NAD27 datum used in Clynne and Muffler (2010).

Major and trace element compositions of bulk tephra can be found in Walowski et al. (2015). Additional data can be found in Clynne et al. (2008); Borg et al. (1997, 2002, 2000); Clynne (1993)

[a] Distance refers to estimated distance from the offshore trench in kilometers

[b] Initial Fe contents used in the calculations were chosen based either on the FeO^T of the bulk tephra or the highest value of FeO^T for MI from a particular cone

[c] CO_2 values represent the highest from each cone after PEC correction and recalculation for melt in equilibrium with Fo_{xx} olivine

[d] H_2O values represent the highest from each cone after PEC correction and recalculation for melt in equilibrium with Fo_{xx} olivine

[e] Refers to the percent olivine required for equilibrium with Fo_{xx} olivine

Table
Click here to download Table: Table 2.pdf

Table 2: Primary Melt Compositions (Trace Element and Isotopic)

Sample	BBL-05	*1 s.d.*	BORG-1	BPB-1	BAS-44-02	BPPC-01	BRVB-01	CC-1	BRM-1
Li	7.2	*0.4*	7.0 *0.8*	7.4 *0.8*	5.4 *1.2*	6.2 *0.3*	11.5 *1.8*	10.4 *0.4*	7.3 *0.6*
B	1.8	*0.4*	3.7 *1.0*	8.3 *0.2*	2.6 *10.1*	3.0 *0.3*	8.0 *0.6*	5.3 *0.3*	3.2 *0.3*
Sc	38	*1.1*	38 *1.5*	34 *0.7*	41 *1.8*	35 *0.7*	32 *0.7*	27 *1.1*	23 *1.4*
V	225	*5*	277 *9*	205 *7*	218 *16*	210 *2*	252 *4*	186 *10*	193 *5*
Rb	5.49	*0.67*	5.44 *0.64*	14.24 *0.54*	4.79 *1.29*	5.07 *0.30*	21.56 *1.46*	15.39 *0.37*	10.43 *0.20*
Sr	270	*10*	438 *8*	476 *41*	408 *12*	450 *11*	454 *5*	342 *25*	1197 *6*
Y	21.2	*0.7*	12.6 *0.4*	15.8 *0.2*	18.6 *1.5*	15.7 *0.4*	18.3 *0.3*	13.1 *0.4*	11.4 *0.2*
Zr	79	*6*	52 *2*	93 *2*	78 *9*	59 *2*	105 *2*	71 *2*	90 *1*
Nb	3.0	*0.4*	2.1 *0.1*	5.6 *0.3*	2.7 *0.5*	1.4 *0.1*	7.0 *0.1*	4.0 *0.1*	5.2 *0.1*
Ba	157	*20*	141 *9*	296 *8*	117 *18*	109 *5*	378 *10*	203 *12*	277 *5*
La	6.2	*0.8*	5.6 *0.3*	11.3 *0.3*	7.4 *0.9*	5.6 *0.2*	14.2 *0.2*	7.5 *0.3*	15.0 *0.1*
Ce	15.9	*1.8*	12.8 *1.0*	24.0 *0.7*	19.6 *1.8*	13.0 *0.5*	34.9 *0.3*	16.9 *0.6*	35.5 *0.3*
Pr	2.20	*0.24*	1.70 *0.10*	3.30 *0.06*	2.68 *0.30*	1.80 *0.06*	4.37 *0.05*	2.31 *0.08*	4.36 *0.02*
Nd	10.80	*0.94*	8.25 *0.54*	13.67 *0.33*	12.38 *1.42*	8.73 *0.26*	19.66 *0.48*	10.52 *0.36*	18.77 *0.14*
Sm	2.77	*0.18*	2.24 *0.14*	3.12 *0.09*	2.91 *0.28*	2.23 *0.14*	4.25 *0.05*	2.41 *0.08*	3.30 *0.06*
Eu	1.04	*0.05*	0.84 *0.02*	1.05 *0.03*	1.01 *0.06*	0.85 *0.03*	1.35 *0.04*	0.80 *0.03*	1.12 *0.02*
Gd	3.50	*0.15*	2.43 *0.15*	3.13 *0.05*	3.19 *0.29*	2.77 *0.14*	3.96 *0.08*	2.47 *0.11*	2.86 *0.03*
Dy	3.80	*0.12*	2.43 *0.09*	2.88 *0.08*	3.01 *0.23*	2.67 *0.07*	3.66 *0.06*	2.55 *0.10*	2.11 *0.23*
Er	2.51	*0.09*	1.40 *0.12*	1.80 *0.07*	2.21 *0.15*	1.81 *0.09*	1.97 *0.11*	1.39 *0.06*	1.24 *0.03*
Yb	2.47	*0.08*	1.37 *0.08*	1.73 *0.08*	2.11 *0.16*	1.73 *0.04*	1.92 *0.05*	1.39 *0.06*	1.27 *0.04*
Hf	1.78	*0.14*	1.35 *0.15*	2.22 *0.09*	1.99 *0.18*	1.71 *0.07*	2.54 *0.17*	1.73 *0.05*	2.33 *0.03*
Ta	0.17	*0.03*	0.11 *0.02*	0.34 *0.01*	0.15 *0.03*	0.08 *0.01*	0.35 *0.02*	0.26 *0.01*	0.23 *0.00*
Pb	1.85	*0.25*	2.26 *0.20*	4.01 *0.14*	1.54 *0.28*	1.62 *0.10*	4.14 *0.41*	3.22 *0.21*	4.81 *0.06*
Th	0.52	*0.07*	0.58 *0.10*	1.75 *0.06*	0.59 *0.09*	0.54 *0.03*	1.77 *0.09*	1.63 *0.06*	1.68 *0.01*
U	0.18	*0.03*	0.29 *0.02*	0.49 *0.02*	0.21 *0.04*	0.18 *0.02*	0.61 *0.04*	0.52 *0.03*	0.49 *0.01*
$^{87}Sr/^{86}Sr$	0.703939		0.703813	0.703877	0.703529	0.703396	0.703985	N/A	0.703080
$^{208}Pb/^{204}Pb$	38.650		38.539	38.612	38.564	38.464	38.646	N/A	38.562
$^{177}Hf/^{176}Hf$	0.283057		0.283055	0.283059	0.283094	0.283052	0.283035	N/A	N/A
$^{143}Nd/^{144}Nd$	0.512859		0.512864	0.512827	0.512948	0.512926	0.512833	N/A	0.512901
[c]$\delta^{11}B$‰ (±1SE)	-4.2(0.9)		-2.6(1.0)	-5.0(0.8)	-4.5(0.8)	-4.9(0.3)	-5.0(0.2)	-10.0(1.0)	-2.4(0.7)
[d]$\delta D_{initial}$ ‰	-85		-90	-80	-70	-75	-75	-95	N/A

Primary melt trace element compositions refer to the average MI composition calculated to be in equilibrium with Fo_{90} olivine for each cone.

Trace element uncertainty calculated as 1 standard deviation of the population used to calculate the average MI composition from each cone (including analytical uncertainty)

Sample names are abbreviations based on Clynne and Muffler (2010), as described in Table 1. Radiogenic isotope analyses are bulk tephra analyses as described discussion section 3

[b] Errors for individual radiogenic isotope compositions can be found in Supplementary Table S2

[c] $\delta^{11}B$ values represent an average from 4-8 MI from an individual vent. See Supplementary Table S3 for details.

[d] δD values from Walowski et al. (2015), measured on the same MI that were analyzed for $\delta^{11}B$.